Cell

Near-infrared spatiotemporal color vision in humans enabled by upconversion contact lenses

Graphical abstract

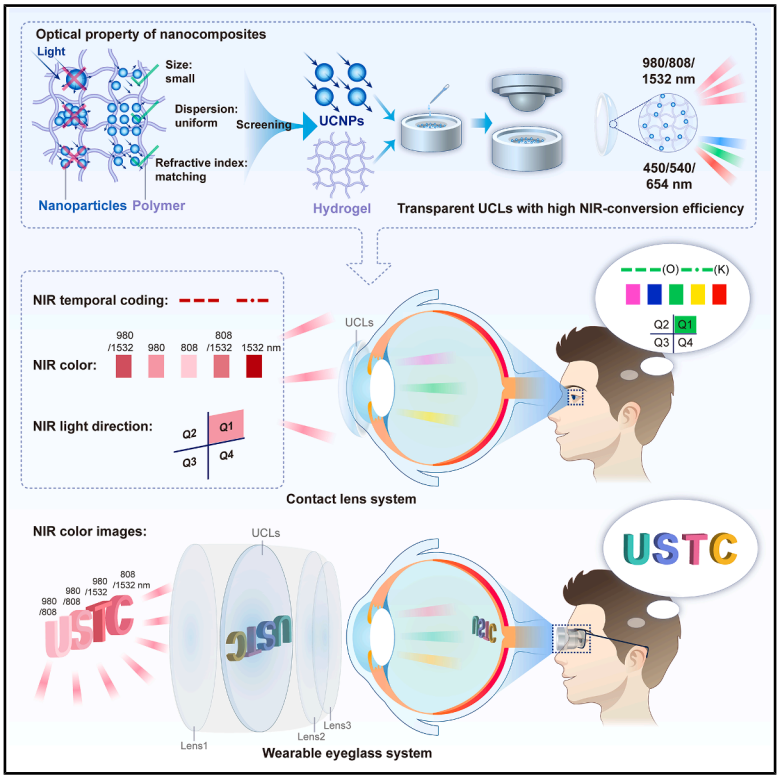

Highlights

- Transparent UCLs with high NIR-conversion efficiency and biocompatibility were developed
- Humans and mice acquire wearable NIR spatiotemporal vision with UCLs
- Humans acquire NIR color vision via trichromatic UCLs converting multispectral NIR light
- Humans can identify the distinct NIR spectra of images by trichromatic UCLs

Authors

Yuqian Ma (马玉乾), Yunuo Chen (陈雨诺), Sheng Wang, ..., Xinglong Gong, Gang Han, Tian Xue (薛天)

Correspondence

mayuqian@ustc.edu.cn (Y.M.), wsh160@ustc.edu.cn (S.W.), zhang_fan@fudan.edu.cn (F.Z.), gongxl@ustc.edu.cn (X.G.), gang.han@umassmed.edu (G.H.), xuetian@ustc.edu.cn (T.X.)

In brief

Based on the principle of refractive index matching, highly transparent upconversion contact lenses (UCLs) with a high concentration of upconversion nanoparticles (UCNPs) were developed. These lenses efficiently convert multispectral near-infrared (NIR) light into the three primary visible colors, enabling humans to acquire wearable NIR color vision.

Ma et al., 2025, Cell *188*, 1–14
June 26, 2025
https://doi.org/10.1016/j.cell.2025.04.019

CellPress

Cell

CellPress

Article

Near-infrared spatiotemporal color vision in humans enabled by upconversion contact lenses

Yuqian Ma (马玉乾),[1,2,6,*] Yunuo Chen (陈雨诺),[1,2,6] Sheng Wang,[3,6,*] Zi-Han Chen,[4,6] Yuanwei Zhang,[5,6] Ling Huang,[5] Xinxin Zhang,[1] Fei Yin,[1] Yunxuan Wang,[1,2] Mingzhu Yang,[4] Zhanjun Li,[5] Kai Huang,[5] Xin Fang,[1,2] Zishuo Li,[1,2] Minghong Wang,[1,2] Wenhui Liu,[1,2] Jia-Nan Li,[1,2] Longfei Li,[1,2] Hang Zhao,[1,2] Min Wei,[1,2] Yiming Shi,[1,2] Rong Liu,[1,2] Mei Zhang,[1,2] Jutao Chen,[1,2] Jiawei Shen,[1,2] Jianjun Meng,[1,2] Yupeng Yang,[1] Fan Zhang,[4,*] Xinglong Gong,[3,*] Gang Han,[5,*] and Tian Xue (薛天)[1,2,7,*]

[1]Department of Ophthalmology, The First Affiliated Hospital of USTC, Hefei National Research Center for Physical Sciences at the Microscale, New Cornerstone Science Laboratory, School of Life Sciences, Division of Life Sciences and Medicine, University of Science and Technology of China, Hefei 230026, China

[2]State Key Laboratory of Eye Health, Institute of Advanced Technology, University of Science and Technology of China, Hefei 230026, China

[3]CAS Key Laboratory of Mechanical Behavior and Design of Materials, Department of Modern Mechanics, University of Science and Technology of China, Hefei 230026, China

[4]Department of Chemistry, Laboratory of Advanced Materials, State Key Laboratory of Molecular Engineering of Polymers, Shanghai Key Laboratory of Molecular Catalysis and Innovative Materials, Fudan University, Shanghai 200433, China

[5]Department of Biochemistry and Molecular Pharmacology, University of Massachusetts Medical School, Worcester, MA 01605, USA

[6]These authors contributed equally

[7]Lead contact

*Correspondence: mayuqian@ustc.edu.cn (Y.M.), wsh160@ustc.edu.cn (S.W.), zhang_fan@fudan.edu.cn (F.Z.), gongxl@ustc.edu.cn (X.G.), gang.han@umassmed.edu (G.H.), xuetian@ustc.edu.cn (T.X.)

https://doi.org/10.1016/j.cell.2025.04.019

SUMMARY

Humans cannot perceive infrared light due to the physical thermodynamic properties of photon-detecting opsins. However, the capability to detect invisible multispectral infrared light with the naked eye is highly desirable. Here, we report wearable near-infrared (NIR) upconversion contact lenses (UCLs) with suitable optical properties, hydrophilicity, flexibility, and biocompatibility. Mice with UCLs could recognize NIR temporal and spatial information and make behavioral decisions. Furthermore, human participants wearing UCLs could discriminate NIR information, including temporal coding and spatial images. Notably, we have developed trichromatic UCLs (tUCLs), allowing humans to distinguish multiple spectra of NIR light, which can function as three primary colors, thereby achieving human NIR spatiotemporal color vision. Our research opens up the potential of wearable polymeric materials for non-invasive NIR vision, assisting humans in perceiving and transmitting temporal, spatial, and color dimensions of NIR light.

INTRODUCTION

Light plays a particularly essential role in conveying a significant amount of external information for living organisms to comprehend the world.[1,2] However, mammals can only perceive a small fraction of the electromagnetic spectrum as visible light, typically in the 400–700 nm range.[3,4] This means that over half of the solar radiation energy, existing as infrared light (>700 nm),[5] remains imperceptible to mammals. The perception limitation in the light spectrum is due to the physical thermodynamic properties of the photon-detecting opsins.[6–9] As a consequence, this leads to a substantial loss of sensory information that could potentially be available. Although tools such as night vision goggles or infrared-visible converters have been used for infrared detection, they require additional energy support and typically cannot distinguish infrared information across multiple spectra. Additionally, each infrared-visible converter requires a multilayer structure, making them opaque and difficult to integrate with the human eye.[10–13] We previously achieved near-infrared (NIR) vision ability in mice by subretinally injecting photoreceptor-binding upconversion nanoparticles (pbUCNPs) into the eyes.[14] Nonetheless, the ocular injection of pbUCNPs may not be readily accepted by humans due to surgical invasiveness.[15,16] Therefore, developing non-invasive NIR vision capabilities with naked eyes to detect multispectral NIR light remains critical and desirable for humans.

Herein, we designed the NIR vision system for humans by integrating upconversion nanoparticles (UCNPs) into soft, non-invasive, and wearable polymeric materials. We modified UCNPs and screened polymeric materials based on refractive index matching and obtained NIR-light upconversion contact lenses (UCLs) with suitable optical properties, hydrophilicity, flexibility,

Please cite this article in press as: Ma et al., Near-infrared spatiotemporal color vision in humans enabled by upconversion contact lenses, Cell (2025), https://doi.org/10.1016/j.cell.2025.04.019

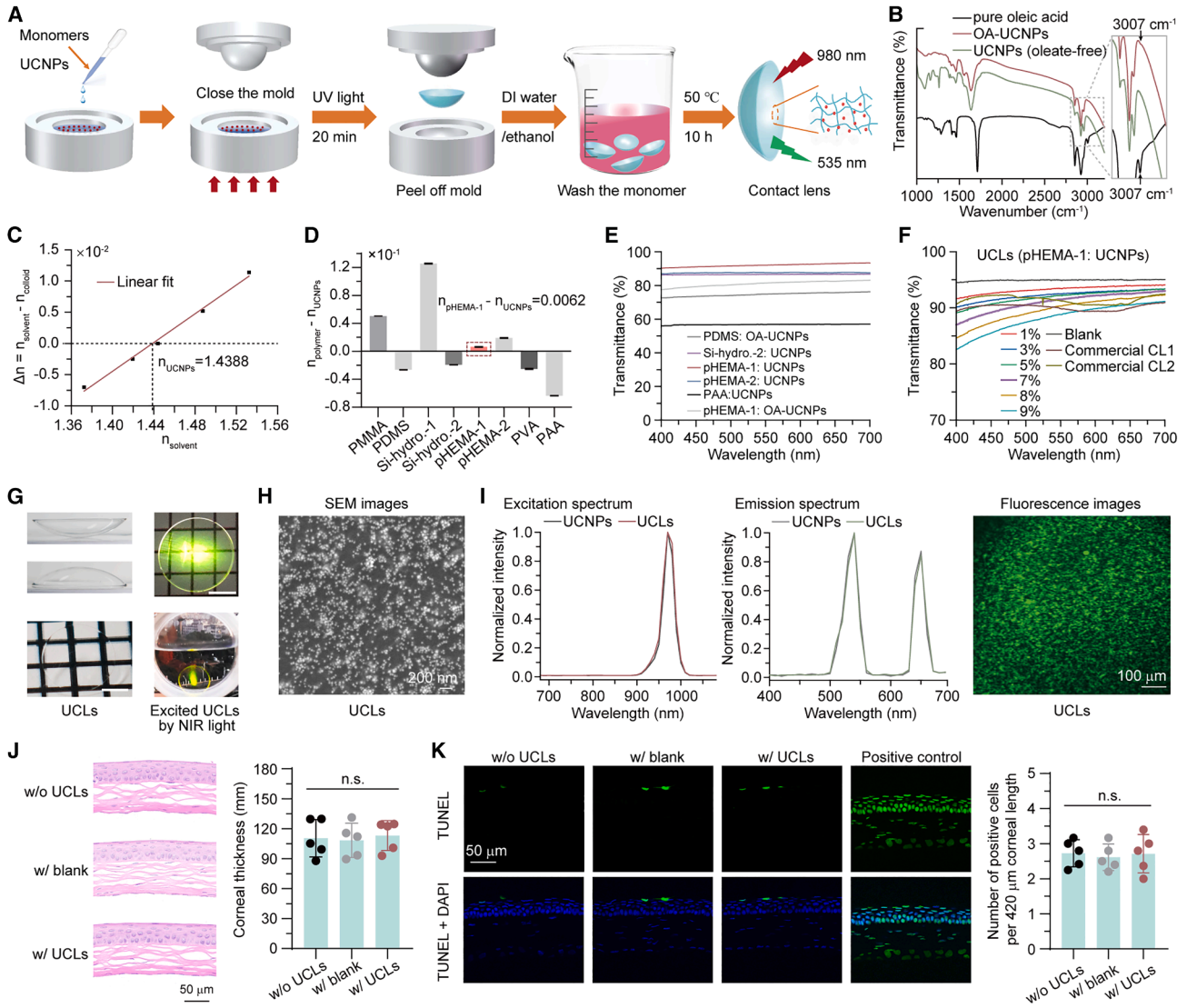

Figure 1. Design and synthesis of soft, wearable, and non-invasive UCLs

(A) Preparation procedures of UCLs. Utilizing the mold of the contact lens, we produced contact lenses with a diameter of 14 ± 0.1 mm, a base curve of 8.5 ± 0.1 mm, and an approximate central thickness of 0.1 mm.

(B) Fourier transform infrared (FTIR) spectra of pure oleic acid, oleate-capped UCNPs, and oleate-free UCNPs in the full range of 1,000–3,500 cm^{-1}. The removal of the oleate ligand from the nanoparticle was revealed by the disappearance of the alkene stretching (C=C) at ~3,007 cm^{-1}.[31] Oleate-capped UCNPs are abbreviated as OA-UCNPs, and oleate-free UCNPs are abbreviated as UCNPs.

(C) Dependence of $\Delta n = n_{solvent} - n_{colloid}$ on the refractive index of the solvent $n_{solvent}$. $n_{colloid}$: refractive index of a colloid solution of oleate-free UCNPs in the solvent. At the instant $\Delta n = 0$, the refractive index of the solvent becomes equal to that of UCNPs.[41]

(D) The refractive index differences between polymers and UCNPs. Data are mean ± SD.

(E) The visible light transmittance of nanocomposites produced using different polymers with OA-UCNPs or UCNPs (3% w/w). Hydrophilic UCNPs or hydrophobic OA-UCNPs were dissolved in a hydrophilic pHEMA-1 polymer, hydrophilic UCNPs were dissolved in a hydrophilic pHEMA-2 polymer, hydrophilic UCNPs were dissolved in a hydrophilic Si-hydrogel-2 polymer, hydrophobic OA-UCNPs were dissolved in a hydrophobic PDMS polymer, and hydrophilic UCNPs were dissolved in a hydrophilic PAA polymer.

(F) The visible light transmittance of the pHEMA-1 contact lenses with varying UCNPs' mass fractions, in comparison to commercial contact lenses. CL, contact lens.

(G) Photos of UCLs and excited UCLs by NIR light. White scale bar: 5 mm.

(H) SEM images of UCLs. The uniform dispersion of UCNPs in the UCLs ensures the suitable optical property and uniform emission of visible light.

(I) Excitation/emission spectra and fluorescence images of UCLs. Visible light was emitted upon the activation of a 980-nm laser source within a two-photon microscope.

(J) Corneal H&E staining and thickness statistics of mice without UCLs, with blank and with UCLs for 6 h. w/o UCLs: without UCLs; w/blank: with contact lens without UCNPs fused; w/UCLs: with UCLs. Data are mean ± SD (two-sided t test; n.s., not significant).

(legend continued on next page)

Please cite this article in press as: Ma et al., Near-infrared spatiotemporal color vision in humans enabled by upconversion contact lenses, Cell (2025), https://doi.org/10.1016/j.cell.2025.04.019

and biocompatibility. With these UCLs, mice could sense the visible light converted from NIR light and distinguish the temporal and spatial information of NIR light. Meanwhile, humans wearing UCLs could accurately recognize NIR temporal information like Morse code and discriminate NIR pattern images. Interestingly, both mice and humans with UCLs exhibited better discrimination of NIR light compared with visible light when their eyes were closed, owing to the penetration capability of NIR light.

In addition to the temporal and spatial information, visual perception can also convey abundant information in the color dimension. Color information in visible light is closely related to its specific wavelength.[17] Infrared light spans a wider range of wavelengths compared with visible light.[18] To distinguish multiple spectra of NIR light, we replaced the conventional UCNPs with trichromatic orthogonal UCNPs that could convert NIR light in three different spectral bands into visible light in three primary colors.[19,20] Through these trichromatic UCLs (tUCLs), we achieved NIR color vision in humans, which could encode more abundant NIR information, focusing specifically on the 800–1,600 nm range. NIR light in this range effectively penetrates biological tissues rich in water, such as eyelids and corneas,[21,22] thereby enhancing NIR vision and biological imaging. Overall, this research enables humans to achieve non-invasive and multi-dimensional NIR image vision without the need for complex external devices. This technology has a wide range of practical applications, including infrared information encoding and transmission, enhanced vision in poor visibility conditions (e.g., foggy or dusty conditions), and integration into smart devices for rescue and emergencies.

RESULTS

UCLs with suitable optical and mechanical properties

In order to achieve human NIR vision through non-invasive, wearable contact lenses, we need to develop polymeric nanocomposites suitable for human eyes. This means that the prepared contact lenses should have suitable optical transparency, hydrophilicity, mechanical properties, and biocompatibility. Currently, soft, transparent polymeric materials have become widely applied in this field.[23,24] However, the fusion of nanoparticles within polymeric materials alters the optical properties of the polymer, making it challenging to obtain high-concentration, optically transparent nanocomposites.[25–27] The optical properties of nanocomposites primarily depend on the light absorption and scattering of nanoparticles within the polymer, which are closely related to the size of the nanoparticles, their dispersion within the polymer, and the matching of their refractive indices (Figure S1A).

To prepare NIR UCLs by incorporating UCNPs into the polymeric materials (Figure 1A), we synthesized Au/$NaGdF_4$: Yb^{3+}, Er^{3+} nanoparticles[28,29] with a diameter of approximately 45 nm (Figure S1B) that exhibited relatively low light transmission loss (absorption and scattering) in the polymeric materials.[30] The majority of polymer materials employed in the contact lenses are hydrophilic, facilitating a comfortable fit between the lens and the cornea of the eye. However, hydrophobic oleic acid residues are often present on the surface of UCNPs. To ensure their uniform dispersion within the polymeric materials, we eliminated the hydrophobic oleic acid residues from the surface of Au/$NaGdF_4$: Yb^{3+}, Er^{3+} nanoparticles[31] (Figure 1B). Even if UCNPs possess an appropriate size and hydrophilicity, the refractive index difference between UCNPs and the polymeric materials still affects the transparency of their composites.[25] We determined that the refractive index of oleate-free UCNPs was 1.4388 (Figure 1C). To match the refractive index of the polymer with it, we conducted a screening of multiple polymers,[32,33] including the hard contact lens material, polymethyl methacrylate (PMMA); soft contact lens materials, polydimethylsiloxane (PDMS) and silicone hydrogel; the commonly used contact lens material, poly (2-hydroxyethyl methacrylate) (pHEMA); as well as other polymeric materials like polyvinyl alcohol (PVA) and polyacrylic acid (PAA). The nanocomposites with a significant refractive index difference between UCNPs and polymeric materials tended to exhibit lower transparency at a 3% mass concentration of UCNPs (Figures 1D, 1E, and S1C). While a hydrophilic pHEMA polymer (pHEMA-1) exhibited the most similar refractive index to oleate-free UCNPs, the transparency of the UCNPs-fused pHEMA-1 nanocomposite exceeded 90%. To achieve high conversion efficiency, we compared the transparency of UCNPs-fused pHEMA-1 UCLs with varying UCNPs mass fractions. We found that at a UCNP mass ratio of 7%, these lenses still displayed suitable optical properties, achieving over 85% transparency in visible light, with the majority of wavelengths exceeding 90% (Figures 1F and 1G). This suggests that we successfully balanced the concentration ratio of UCNPs in the UCLs and their optical properties. Through Ashby plot analysis, UCLs represent the highest level in terms of particle doping ratio and optical performance compared with various reported UCNP/polymer nanocomposites[19,34–40] (Figure S1D).

Meanwhile, in the scanning electron microscopy (SEM) images of UCLs, the zeta potential (-16 ± 1.2 mV) and the hydrodynamic size distribution of UCNPs in mixed solutions indicate that UCNPs fused well, were stable, and dispersed uniformly within the UCLs (Figures 1H, S1E, and S1F). This fusion process did not change the excitation and emission spectra of UCNPs in the UCLs, allowing them to emit a uniform green light upon NIR-light excitation (Figure 1I). The addition of UCNPs also had no impact on the hydrophilicity and water content of UCLs, comparable to commercial contact lenses (Figures S1G and S1H). The results of rheological tests on UCLs using shear modulus and shear cyclic loading revealed that they displayed similar flexibility and reliable fatigue resistance compared with commercial contact lenses (Figure S1I). The experiment on tensile modulus further confirmed the suitable mechanical stability of UCLs

(K) Detection of corneal apoptosis by TUNEL (terminal deoxynucleotidyl transferase dUTP nick end labeling) staining. Strong TUNEL signals were observed in the DNase I-dealt corneas of mice (positive control), but a few were observed in the corneas of mice without UCLs/with blank/with UCLs for 6 h. Green, TUNEL staining; blue, DAPI. The number of positive cells per 420 μm corneal length was counted. Data are mean ± SD (two-sided t test; n.s., not significant).
See also Figures S1 and S2.

Please cite this article in press as: Ma et al., Near-infrared spatiotemporal color vision in humans enabled by upconversion contact lenses, Cell (2025), https://doi.org/10.1016/j.cell.2025.04.019

(Figure S1J). The intensities of 980 nm light absorbed and visible light emitted after passing through UCLs under different intensities of incident 980 nm light indicate the quantitative conversion of NIR light to visible light through UCLs (Figure S1K). Overall, the suitable mechanical properties and efficient upconversion capabilities of soft UCLs are appropriate for human wearing and human NIR vision.

Biocompatibility of UCLs

We then assessed the *in vivo* biocompatibility and potential side effects of the UCLs. After a single 6-h wearing in a short period, we found that the number of cell layers in the cornea and retinal outer nuclear layer did not differ between mice with or without UCLs through hematoxylin and eosin (H&E) staining (Figures 1J and S2A). Sparse signals of cell apoptosis were observed on the corneas in all groups, suggesting the wearing of UCLs did not increase the risk of corneal cell apoptosis (Figure 1K). The staining of microglia marker Iba1 showed that there was no microglia aggregation, suggesting no inflammation response in retinae of all groups (Figure S2B). For long-term toxicity tests, mice wore the UCLs for durations of 3, 7, or 14 consecutive days (6 h per day). We found that wearing contact lenses for 3, 7, and 14 days did not cause any changes in corneal thickness, retinal morphology, or retinal inflammation response. However, continuous wearing of either commercial contact lenses or UCLs led to a slight increase in corneal cell apoptosis after 7 and 14 days of wearing (Figures S2C and S2D). This could be attributed to the mechanical friction caused by wearing contact lenses. However, UCLs did not exacerbate this effect. Taken together, these results suggest that UCLs have good biocompatibility without detectable side effects on the corneas and retinae of mice.

NIR-mediated light sensation of mice with UCLs

After confirming the favorable biocompatibility of the UCLs, we proceeded to validate whether NIR light could effectively activate the visual system of mice through these UCLs. We performed the *in vitro* suction pipette recordings on the acutely dissected mouse retina, which was flat-mounted on a UCL disk (Figure S3A). Rod photocurrents were elicited by the 980-nm light pulse only with the UCL disk presented, and the amplitudes and dynamics were consistent with those activated by 535-nm visible light (Figures S3B–S3D). The *in vivo* electroretinography (ERG) recordings showed that wearing these UCLs had no effect on the ERG signals mediated by visible light, suggesting that UCLs did not interfere with normal vision with their high transparency (Figures 2A and 2B). Meanwhile, ERG signals evoked by NIR light in mice with UCLs exhibited a similar response pattern with those evoked by visible light. Whereas, in mice without UCLs, NIR light could not evoke any ERG signals.

Then, we investigated NIR-mediated light sensation in mice with UCLs at the behavioral level. The UCLs were secured onto the eyes of moving mice by an eyelid suture. To detect the pupil light reflex, we monitored the contralateral eye's pupil size while the eye with UCLs was illuminated by NIR light (Figure 2C). When mice wore UCLs, NIR light induced the pupillary constriction, while no response was observed in mice without UCLs (Figures 2C and 2D). In addition to subconscious pupillary light reflex behavior, we also investigated whether mice with UCLs could consciously sense NIR-converted visible light. Mice with UCLs displayed a preference for the dark box over NIR-light box in the light-dark box assay and mice without UCLs could not (Figures 2E and 2F). In the light-induced fear-conditioning experiment, NIR light also could induce the freezing behavior in mice with UCLs but not in mice without UCLs (Figures 2G and 2H). These results indicate that mice with UCLs can acquire NIR-mediated light sensation ability.

In aforementioned NIR vision behavior tests, although the eyelids were sutured, NIR light could readily induce behavior responses in mice with UCLs, whereas visible light could not induce significant responses (Figures 2F and 2H). A potential explanation for this was that NIR light could penetrate the eyelids easily.[42,43] We measured the transmittance of the mouse eyelids of 535- and 980-nm light (Figure 2I). The results showed that the transmittance of the mouse eyelids of 535-nm light was 0.388%, while that of 980-nm light was 23.292%. This demonstrates that NIR-light information can be transmitted stealthily even through closed eyes.

NIR-light information recognition of mice with UCLs

Other than innate behaviors induced by NIR-mediated light sensation, we further investigated whether mice with UCLs could recognize NIR light's spatial and temporal information. We recorded the visually evoked potential (VEP) at four different locations in the primary visual cortex of mice when the contralateral eyes were illuminated by visible light or NIR light (Figure 3A). As anticipated, wearing UCLs did not affect visible light-induced VEP signals. Meanwhile, we could record VEP signals in mice with UCLs under NIR-light illumination, but no signals were detected in mice without UCLs (Figures 3A and 3B). The amplitude and response time of VEP signals evoked by NIR light were consistent with those evoked by visible light.

Additionally, we performed intrinsic optical imaging of the primary visual cortex (V1).[44,45] NIR and visible light grating stimulations at three different visual fields elicited well-separated intrinsic optical signals in the visual cortex of mice with UCLs (Figures 3C–3E and S3E). These well-separated V1 retinotopic responses indicated that spatial information of NIR light could be transmitted directly to the mouse visual cortex.[46] In the conditioned place-avoidance experiment,[47,48] mice could distinguish NIR flickering light with two different frequencies (2 and 0.4 Hz) and made correct behavioral decisions to avoid being shocked (Figures 3F–3H, S3F, and S3G). These findings illustrate that NIR vision facilitated by UCLs enable mice to perceive NIR spatial and temporal information.

NIR vision of humans with UCLs

Having achieved non-invasive NIR vision in mice through the UCLs, we applied the UCLs to humans. Sensitivity tests for human perception of visible and NIR light were conducted in the dark or in ambient light conditions (Figures 4A and 4C). We observed no differences in the perception sensitivity to visible light in humans with or without UCLs, indicating that highly

Please cite this article in press as: Ma et al., Near-infrared spatiotemporal color vision in humans enabled by upconversion contact lenses, Cell (2025), https://doi.org/10.1016/j.cell.2025.04.019

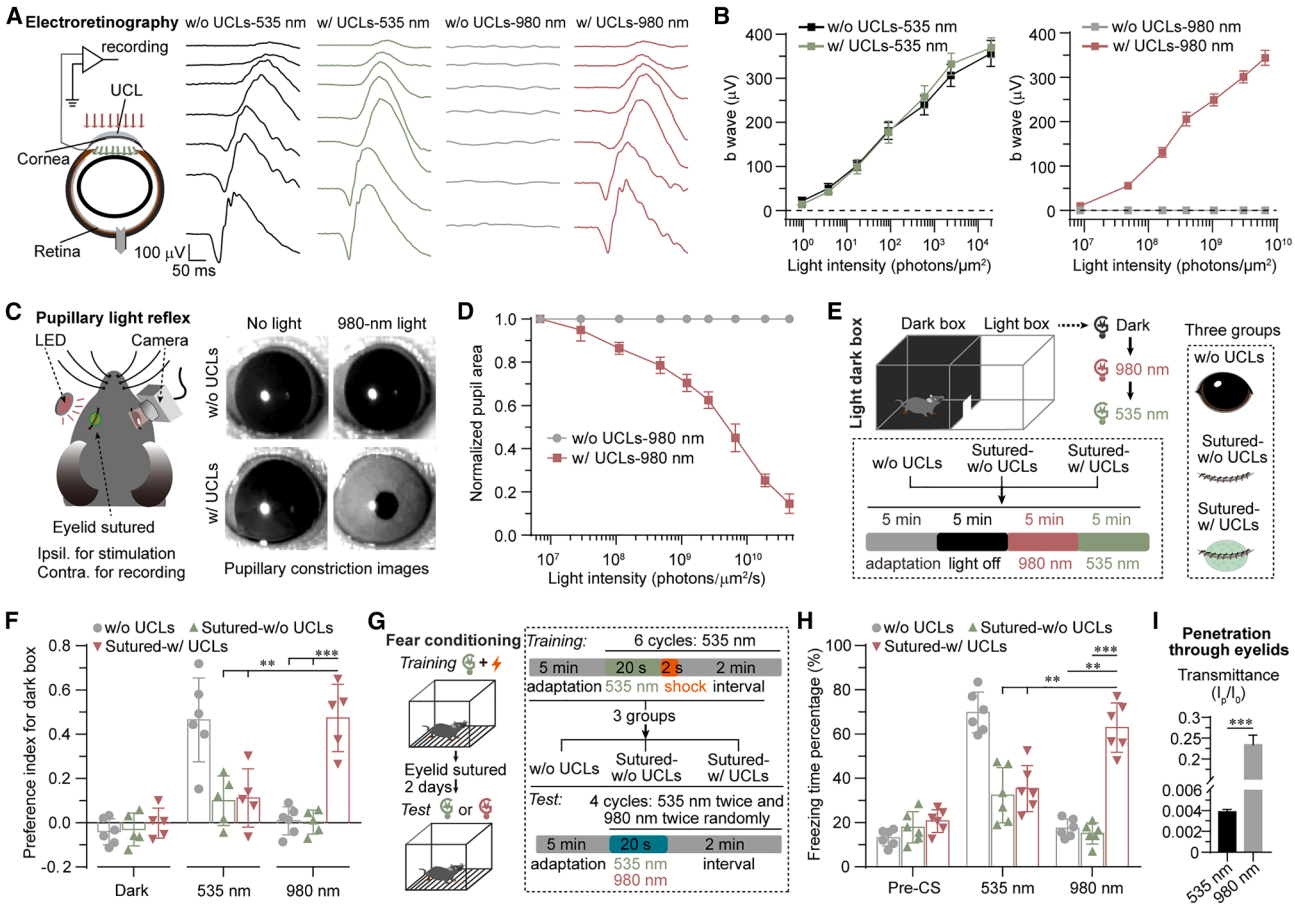

Figure 2. NIR-mediated light sensation of mice with UCLs

(A) ERG diagram and representative response traces. The UCL was attached to the cornea of the mouse and then response signals were recorded. A series of ERG responses were induced by 20-ms flashes of 535- or 980 nm at different intensities. Data were lowpass filtered at 50 Hz and sampled at 5 kHz.

(B) Intensity-response curves of ERG in mice with or without the UCLs under 535- or 980-nm light stimulation. Data are mean ± SEM (without UCLs, 535 nm: $n = 7$; with UCLs, 535 nm: $n = 9$; without UCLs, 980 nm: $n = 6$; with UCLs, 980 nm: $n = 9$).

(C) Pupillary light reflex mediated by NIR light. One eye of each mouse was sutured with the UCLs placed inside and exposed to 980-nm light stimulation, and the other eye was not sutured for pupillary size detection. Images show pupillary constriction of mice with or without UCLs under 980-nm light stimulation. The power intensity of 980-nm light: 4.45×10^{10} photons/μm^2/s.

(D) Dose-response curves of normalized pupillary constriction under 980-nm light stimulation. Mice with or without UCLs, $n = 5$ for all; data are mean ± SD.

(E) Diagram of light-dark box experiment.

(F) Preference index for dark box under three different light box conditions (dark, 980 nm, and 535 nm). Preference index = (time spent in dark box − in light box)/(time spent in dark box + in light box). Light power intensities of the 980- and 535-nm light at the center of the box were 6.03×10^9 and 3.16×10^3 photons/μm^2/s, respectively. Data are mean ± SD (two-sided t test; $0.001 < **p < 0.01$, $***p < 0.001$).

(G) Diagram of light-induced fear-conditioning experiment.

(H) Freezing time percentage during 20 s "pre-CS," 535-nm, and 980-nm light stimulation. "Pre-CS": before conditioned stimulation, a 20-s period of adaptation right before light stimulation onset; CS, conditioned stimulation (light stimulation). 535- or 980-nm light stimulation each occurred 2 times randomly. Light power intensities of the 980- and 535-nm light at the center of the box were 4.32×10^9 and 2.76×10^3 photons/μm^2/s, respectively. Data are mean ± SD (two-sided t test; $0.001 < **p < 0.01$, $***p < 0.001$).

(I) Transmittance of 535- and 980-nm light through mouse eyelid tissue. I_0, the intensity of direct light; Ip, the intensity of penetrating light. Data are mean ± SD (two-sided t test, $n = 3$, $***p < 0.001$).

See also Figure S3.

transparent UCLs did not impact normal human vision (Figures 4B and 4D). Participants wearing UCLs were able to identify NIR light in the dark room (Figure 4B). When participants closed their eyes, their sensitivity to NIR light remained almost unchanged, but the sensitivity to visible light decreased over 200-fold. This was attributed to the better penetration ability of NIR light through the eyelid, as previously demonstrated in mice (Figures 2E–2I). Moreover, in ambient light condition (100, 200, and 300 lux), participants were still able to perceive NIR light (Figures 4C, 4D, S3H, and S3I), indicating that NIR vision via UCLs was ambient-daylight compatible and existed in parallel with native daylight vision. Interestingly, under an

Please cite this article in press as: Ma et al., Near-infrared spatiotemporal color vision in humans enabled by upconversion contact lenses, Cell (2025), https://doi.org/10.1016/j.cell.2025.04.019

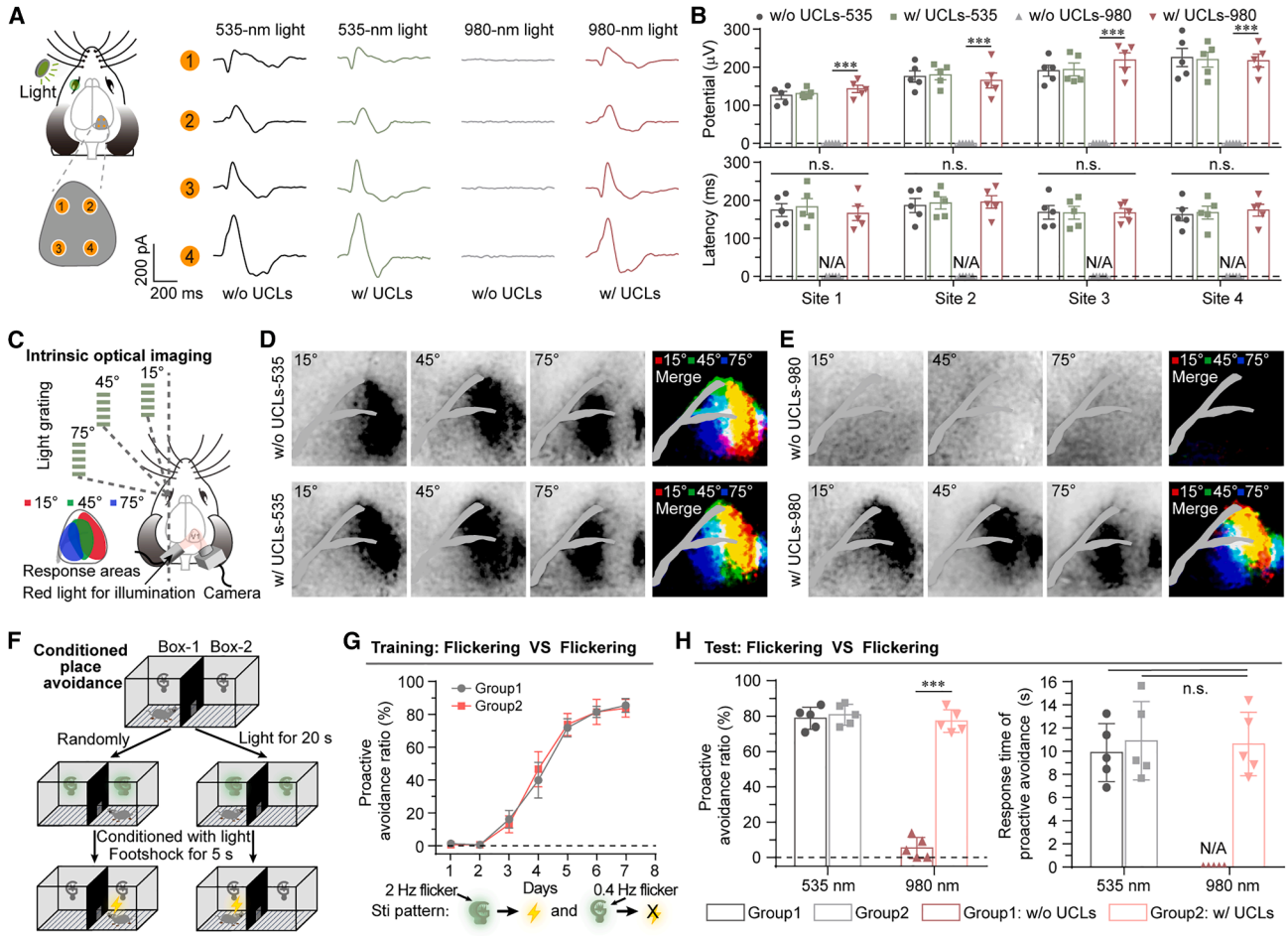

Figure 3. NIR-light information discrimination of mice with UCLs

(A) Diagram of visual evoked potential (VEP) recording and the corresponding VEP traces. One eye of mice with or without UCLs was illuminated by 535- (5.27×10^3 photons/μm^2/s) or 980-nm light (4.88×10^9 photons/μm^2/s), and VEP signals at the four sites in the contralateral primary visual cortex were recorded. Data were lowpass filtered at 50 Hz and sampled at 5 kHz.

(B) Amplitudes and latency time of peak VEPs. Data are mean ± SEM, two-sided t test; ***$p < 0.001$; n.s., not significant; N/A, not applicable.

(C) Diagram of intrinsic optical imaging. Intrinsic optical signals in primary visual cortex (V1) were recorded while contralateral eyes were stimulated by moving rectangular grating of 535- (4.56×10^3 photons/μm^2/s) or 980-nm light (6.53×10^9 photons/μm^2/s) at three different visual angles.

(D and E) The corresponding signals in V1 of mice under 535- or 980-nm light stimulation. Signal pictures are the top view on the right V1 cortex of presented mice. Overlapping images of intrinsic optical signals are annotated with color to differentiate the responses at three distinct visual angles.

(F) Diagram of conditioned place-avoidance experiment. Light power intensities of 535- and 980-nm light at the center of the box were 2.36×10^3 and 5.08×10^9 photons/μm^2/s, respectively.

(G) Proactive avoidance ratio of mice during the visible light training stage. In this experiment, two light stimulations were employed: 2 and 0.4 Hz flickering light. The 2 Hz flickering light was associated with electric shock, whereas the 0.4 Hz flickering light was associated with no shock. "Proactive avoidance" refers to the situation where mice move from the punished box into another unpunished box depending on the stimulation and successfully avoid being shocked (refer to Figure S3F). Proactive avoidance ratio = times of avoiding being shocked successfully/times of situations where mice were in the punished box when light stimulation started. Data are mean ± SD.

(H) Proactive avoidance ratio and response time of mice during the visible light and NIR light test stage. The stimulation pattern is the same as that in (G). The response time is defined as the interval between the initiation of light stimulation and the moment when the mice fully move into another box. Data are mean ± SD; two-sided t test; n.s., not significant; ***$p < 0.001$.

See also Figure S3.

ambient light background, the sensitivity to NIR light increased by 3.7-fold when participants closed their eyes, while the sensitivity to visible light decreased by 4.5-fold (Figure 4D). This could be explained by the closed eyes reducing ambient visible light input while increasing the signal-to-noise ratio of NIR-light detection.

We then measured the NIR vision flicker fusion frequency of humans with UCLs and found that it was similar to that of visible light vision (Figure 4E). On this basis, we used the NIR flickering light to implement temporal coding and found that participants with UCLs could accurately distinguish the letter sequences coded by NIR flashes (Figure 4F). In the spatial information

Please cite this article in press as: Ma et al., Near-infrared spatiotemporal color vision in humans enabled by upconversion contact lenses, Cell (2025), https://doi.org/10.1016/j.cell.2025.04.019

CellPress

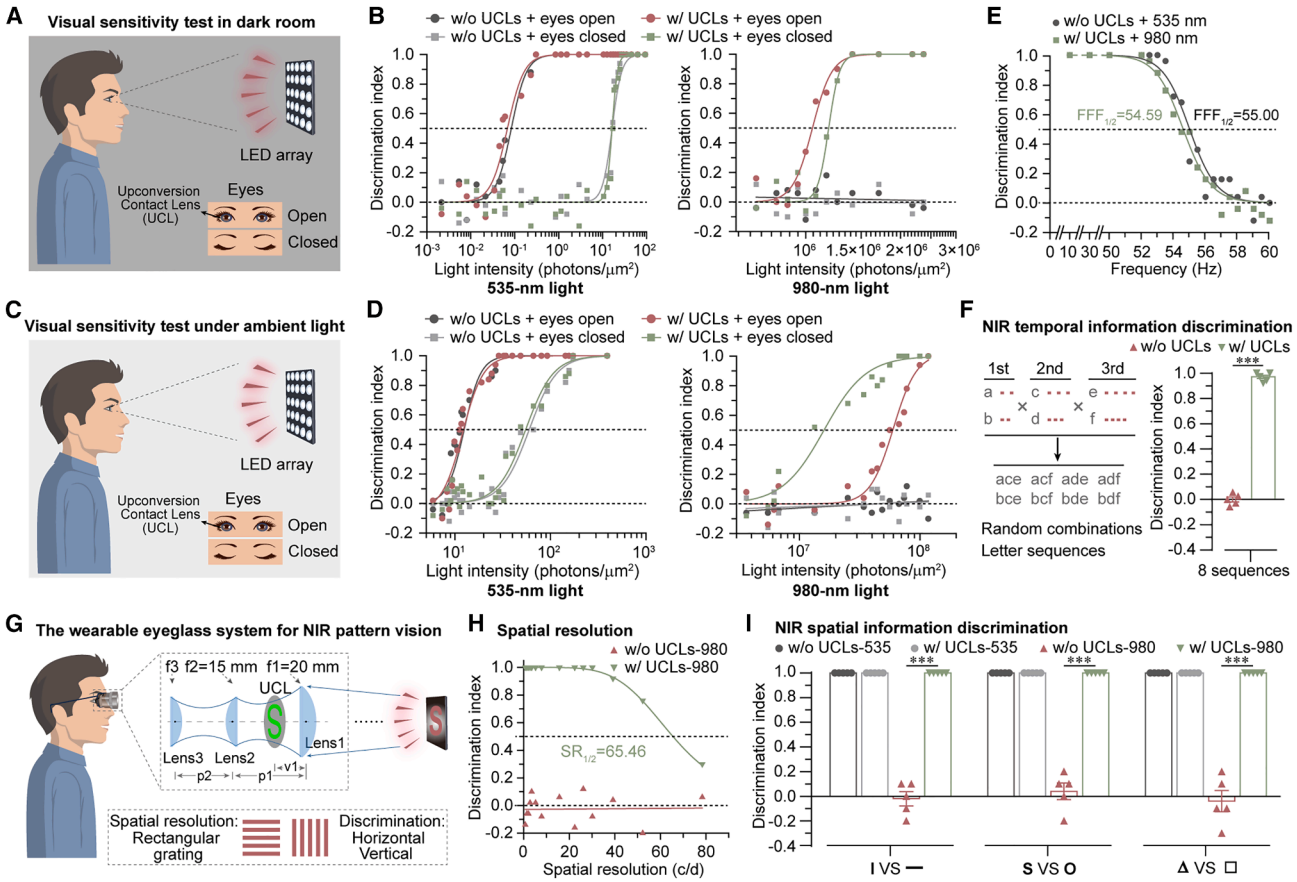

Figure 4. NIR vision of humans with UCLs

(A) A schematic diagram depicting the visual sensitivity test in a dark room. Human participants were instructed to fixate on an LED array in a dark room. The experiment consisted of four distinct conditions, including the eyes-open state without UCLs, the eyes-closed state without UCLs, the eyes-open state with UCLs, and the eyes-closed state with UCLs.

(B) Visual sensitivity to light power intensity of visible light and NIR light in a dark room. Discrimination index assesses how much a participant's actual accuracy deviates from the expected accuracy in random guessing, indicating their performance relative to chance. Hill function fitting is employed to analyze the average discrimination index across various light power intensities.

(C) A schematic diagram depicting the visual sensitivity test under ambient light (100 lux).

(D) Visual sensitivity to light power intensity of visible light and NIR light under ambient light.

(E) Flicker fusion frequency (FFF) of participants without UCLs under visible light and with UCLs under NIR light. $FFF_{1/2}$ represents the frequency at which the discrimination index is 0.5, indicating the threshold for FFF.

(F) The discrimination index of participants for NIR temporal information. Variations in stimulation frequency and the number of flashes were employed as encoding parameters for different letters like Morse code. 8 letter sequences were discriminated. Data are mean ± SEM; two-sided t test, $^{***}p < 0.001$.

(G) A schematic diagram depicting the detection of spatial resolution (SR) and the discrimination of NIR pattern images. Participants distinguished light gratings and paired pattern images at a certain distance of ~70 cm from their eyes with the wearable eyeglass system. The system comprised three plano-convex lenses and a built-in flat UCL integrated into the optical path. The focal length f1 of lens 1 was 20 mm, while the focal lengths f2 and f3 of lens 2 and lens 3 were both 15 mm. The distance between the focal points of lens 1 and lens 2, denoted as p1, was 52.06 mm, while the distance between the focal points of lens 2 and lens 3, denoted as p2, was 43.26 mm. The distance between the flat UCL and the focal point of lens 1, denoted as v1, was 20.69 mm, and it could also be adjusted based on the object distance.

(H) Spatial resolution of participants through NIR vision. $SR_{1/2}$ represents the spatial resolution at which the discrimination index is 0.5, indicating the threshold for spatial resolution.

(I) The discrimination index of participants for NIR pattern images. Data are mean ± SEM; two-sided t test, $^{***}p < 0.001$.

See also Figure S3.

recognition of NIR light, UCLs cannot achieve fine image perception from an optical principle standpoint. This is because the NIR light, which originally carried spatial information for imaging, is converted into scattered visible light before entering the human eye, altering the spatial information carried by the direction of light propagation. However, participants with UCLs exhibited the ability to recognize coarse NIR images, such as distinguishing the direction of NIR light coming from specific visual quadrants (Figure S3J). To achieve fine NIR image vision, we developed a wearable eyeglass system consisting of three

Please cite this article in press as: Ma et al., Near-infrared spatiotemporal color vision in humans enabled by upconversion contact lenses, Cell (2025), https://doi.org/10.1016/j.cell.2025.04.019

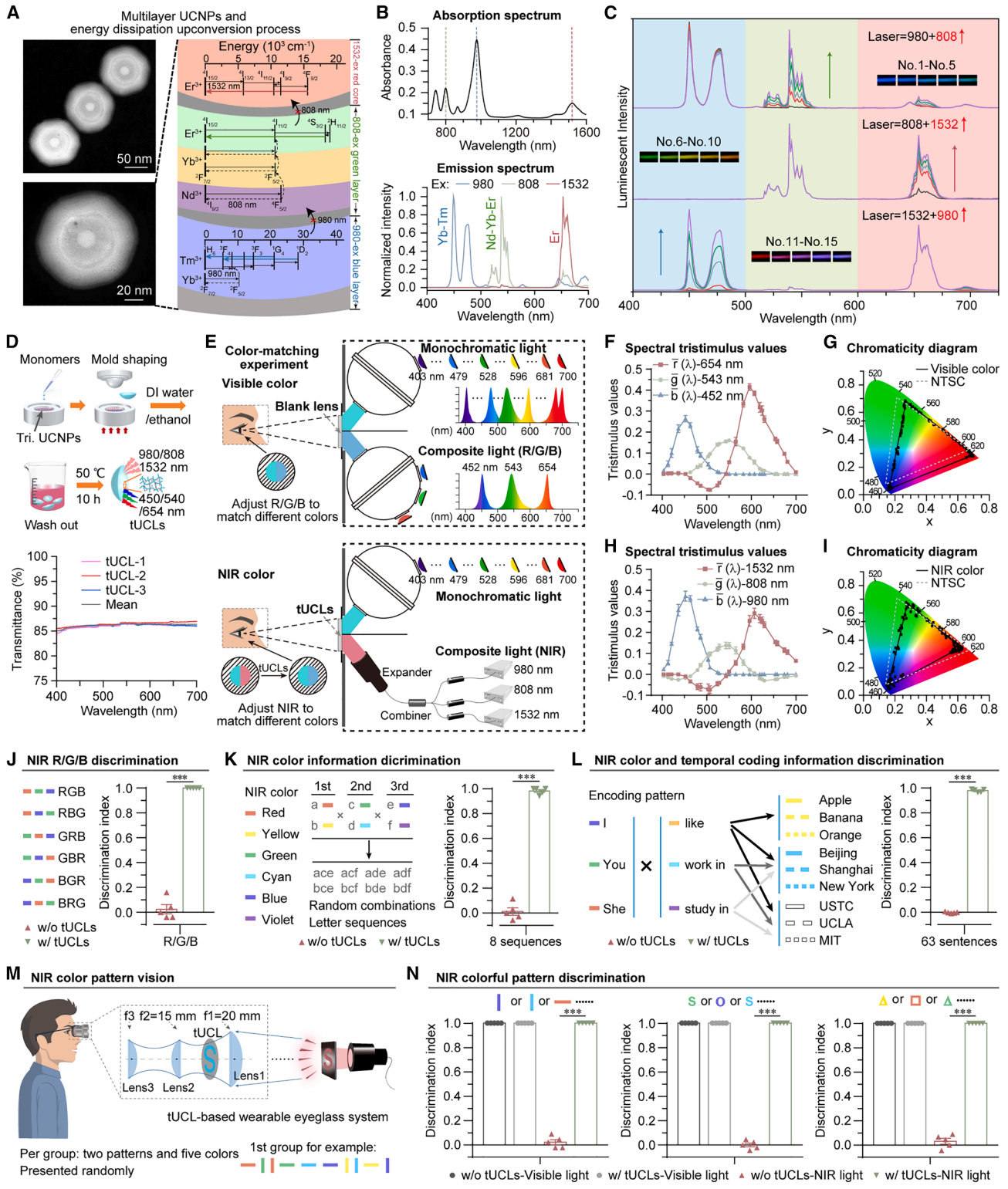

Figure 5. NIR color vision of humans with tUCLs

(A) The trichromatic upconversion mechanism of NIR light. The high-angle annular dark-field scanning transmission electron microscopy (HAADF-STEM) images of the synthesized trichromatic UCNPs are shown. In view of the different contents of Yb^{3+} needed for green (Er^{3+}) and blue (Tm^{3+}) emission, Nd^{3+} ions could be introduced into the intermediate layer to absorb 808 nm photons and generate green emission, while the outer shell was set to absorb 980-nm photons and

(legend continued on next page)

Please cite this article in press as: Ma et al., Near-infrared spatiotemporal color vision in humans enabled by upconversion contact lenses, Cell (2025), https://doi.org/10.1016/j.cell.2025.04.019

convex lenses and a built-in flat UCL integrated into the optical path (Figure 4G). With this system, participants could distinguish the NIR moving gratings with a spatial resolution threshold of ~65 cycles per degree (c/d) (Figure 4H). Moreover, we demonstrated that participants with the UCLs were able to discriminate NIR pattern images (horizontal and vertical lines, S and O shapes, triangle and square) (Figure 4I). Taken together, these findings show the potential of UCLs for NIR-light information discrimination in both temporal and spatial dimensions in humans.

NIR color vision of humans with tUCLs

To perceive infrared light with the multi-spectra that widely exist in the natural environment, we used trichromatic UCNPs with multi-wavelength conversion capabilities[19,20] to replace the conventional UCNPs. We synthesized trichromatic orthogonal UCNPs with multiple NIR absorption-emission layers (Figures 5A and S4A–S4H). These UCNPs exhibited efficient absorption of NIR light at peak wavelengths of 808, 980, and 1,532 nm, while emitting visible light at peak wavelengths of 540, 450, and 650 nm, respectively (Figure 5B). These emission peaks corresponded to the three primary colors of green, blue, and red for humans. As expected, a single NIR excitation from this trichromatic orthogonal UCNPs could generate a relatively singular emission band (Figures 5A and 5B), thereby avoiding interference issues in the emission spectral bands compared with the direct mixture of three different conventional UCNPs. Indeed, in dual-spectral NIR-light excitation experiments, independently adjusting the intensities of NIR light at one spectrum could alter trichromatic UCNPs' visible light emission at the corresponding spectrum, suggesting their suitable trichromatic conversion capabilities and color separation (Figures 5C and S4I–S4Q).

Furthermore, we integrated the trichromatic orthogonal UCNPs (oleate-free) into pHEMA contact lenses and found that these contact lenses also had good transparency at a 7% mass fraction level (Figure 5D). To assess the effectiveness of the tUCLs in facilitating human NIR color visual perception, a color-matching experiment was conducted.[50–54] During visible color matching, participants were tasked with adjusting the proportion of red/green/blue (R/G/B) light in visible composite light to match the color of various monochromatic lights at different peak spectra (403–700 nm) (Figures 5E, S5, S6A, and S6B). The R/G/B proportions in the visible composite light matching the color of each monochromatic light were presented as the spectral tristimulus values and the color space in the chromaticity diagram (Figures 5F and 5G). Similarly, through the tUCL conversion, participants adjusted the proportion of NIR light at three different spectra to match the color of various monochromatic lights (Figures 5E, S5, S6A, and S6B). We determined the tristimulus values of NIR light at three different spectra in the NIR composite light that matched the color of each monochromatic light and showed the NIR color space perceivable by humans (Figures 5H and 5I). The results showed that participants with tUCLs could effectively recognize NIR light with three wavelengths and perceive multiple NIR colors by adjusting the proportions of three NIR primary colors (Figures 5H and 5I). The spectral tristimulus values of the NIR light were similar to those of visible light (Figures 5F and 5H), except for minor discrepancies, which was possibly due to the UCNPs' emission leakage at non-primary wavelengths (Figure 5B). Likewise, the color space of the perceived NIR composite light on the color chart was highly similar to that of visible light and the National Television Standards Committee (NTSC) standard (Figures 5G and 5I). It indicates that human NIR color vision can be effectively achieved by tUCLs

generated blue emission. Specifically, Yb^{3+} ions in the outer shell could act as two roles, the sensitizers to transfer energy to Tm^{3+} ions[49] and the shield to avoid Yb^{3+} ions in the intermediate shell absorbing 980-nm photons.

(B) The absorption spectrum in the NIR region (750–1,600 nm) and the emission spectra in the visible region (400–700 nm) of trichromatic UCNPs.

(C) The trichromatic upconversion emission spectra were regulated by adjusting laser power under dual excitation (combinations, 980 + 808, 808 + 1,532, and 1,532 + 980 nm; inset, the corresponding photographs of trichromatic UCNPs).

(D) The preparation process and visible light transmittance of tUCLs. These tUCLs possess the capability to convert NIR light at three wavelengths and exhibit high transparency.

(E) A schematic diagram of color-matching experiment. Participants were required to observe a circular board with either a blank lens (without UCNPs) or a flat tUCL placed in front of them within a 2° visible angle range. Integrating spheres and white frosted film were used to ensure that the LED light was uniform. Three monochromatic LEDs (R, 654 nm; G, 543 nm; B, 452 nm) or three types of lasers with different wavelengths (1,532, 808, and 980 nm) were employed as the adjustable composite light, aiming to achieve color matching with a series of monochromatic LED lights in the range of 400–700 nm. These three types of lasers were combined into a single laser beam through the utilization of a fiber beam combiner and enlarged into a uniform spot using a beam expander to ensure consistent optical performance.

(F and G) The spectral tristimulus values, and the composite visible color space in the chromaticity diagram measured by visible color matching.

(H and I) The spectral tristimulus values, and the composite NIR color space in the chromaticity diagram measured by NIR color matching. The related luminance and chroma values of a series of monochromatic and composite lights were measured, recorded, and analyzed as described in Figure S5.

(J) The discrimination index of participants for NIR R/G/B. Data are mean ± SEM; two-sided t test, $^{***}p < 0.001$.

(K) The discrimination index of participants for NIR color information. Here, these six composite colors were used to encode different letters, which could be encoded into 8 sequences. Data are mean ± SEM; two-sided t test, $^{***}p < 0.001$.

(L) The discrimination index of participants for NIR color and temporal coding information. Herein, six distinct colors were utilized to encode subject or predicate words, while object words were encoded using a combination of three colors and various temporal frequencies (1, 2, and 4 Hz). Corresponding words could be used to encode a complete sentence. In this experiment, 63 sentences were encoded. Data are mean ± SEM; two-sided t test, $^{***}p < 0.001$.

(M) A schematic diagram of NIR color pattern vision experiment. Participants distinguished paired colorful pattern images at a certain distance of ~70 cm from their eyes with the wearable eyeglass system. The aforementioned five composite colors and three pairs of pattern images (━ vs. ┃, S vs. O, △ vs. □) were used for the tests.

(N) The discrimination index of participants for NIR colorful pattern images. Data are mean ± SEM; two-sided t test, $^{***}p < 0.001$.

See also Figures S4, S5, and S6.

Please cite this article in press as: Ma et al., Near-infrared spatiotemporal color vision in humans enabled by upconversion contact lenses, Cell (2025), https://doi.org/10.1016/j.cell.2025.04.019

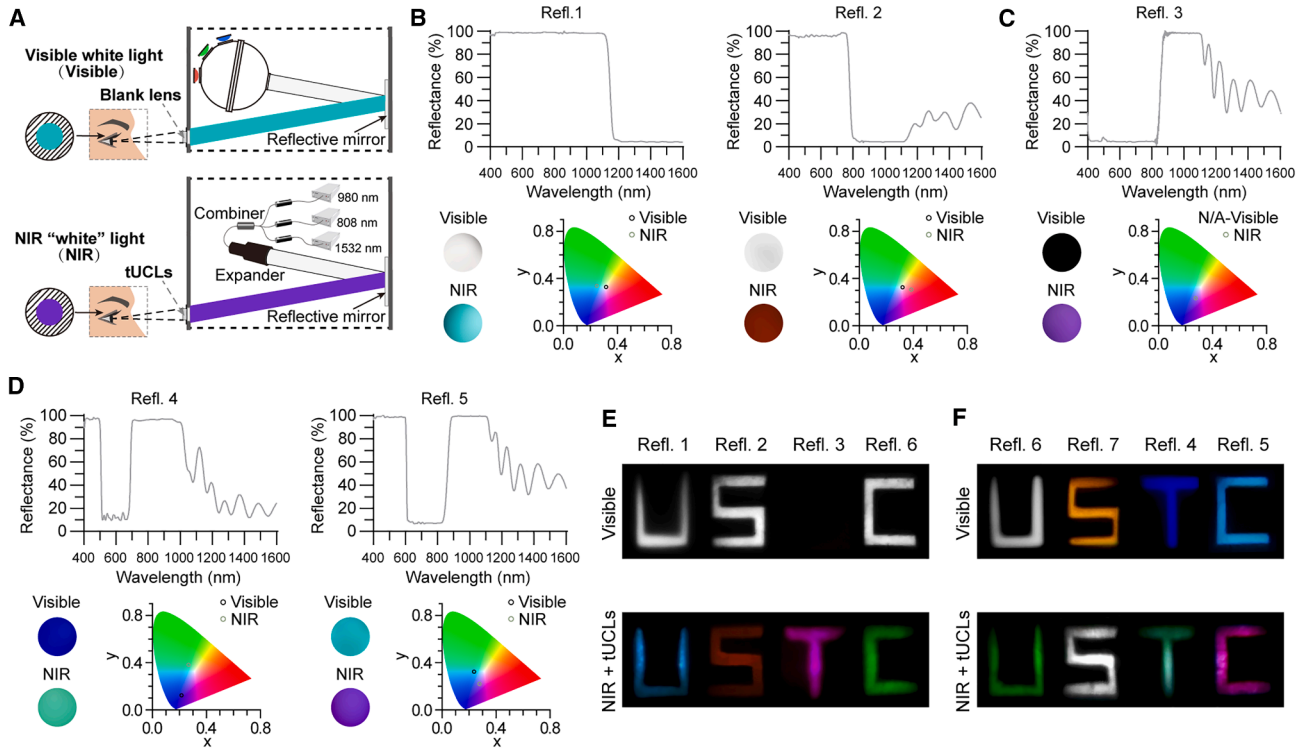

Figure 6. Colorful reflective image under NIR light

(A) A schematic diagram of the reflective color experiment. Reflective mirrors with different reflection spectra were used to emit visible white light or NIR "white" light. A participant or camera was used to detect the color information of the reflected light.

(B–D) The reflection spectra of different reflective mirrors, the photographs displayed under visible white light and NIR white light, and the chromaticity coordinates on the chromaticity diagram. N/A, not applicable.

(E) Letter patterns composed of some reflective mirrors. These letters appeared white and black under visible white light but revealed diverse color information under NIR white light.

(F) Letter patterns composed of other reflective mirrors. These letters revealed diverse color information under both visible and NIR white light. In this experiment, we observed these letter patterns using the wearable eyeglass system.

See also Figure S6.

with non-interfering, orthogonal, and multispectral conversion properties.

With the NIR color recognition ability, participants with tUCLs could discriminate the letter sequences encoded by NIR color (Figures 5J and 5K). This indicates that by incorporating the NIR color dimension, more abundant information can be coded and transmitted. Additionally, through the combination of color and temporal information, participants with tUCLs could accurately interpret coded sentences with NIR light (Figure 5L). We also verified that participants with tUCLs could recognize various colorful NIR pattern images with the wearable eyeglass system (Figure 4G), including colored horizontal and vertical lines, S and O shapes, triangle and square (Figures 5M and 5N). These results demonstrate that our nanocomposite materials can enable humans to obtain multispectral NIR visual information.

Colorful reflective images under NIR light

Typically, most of the images we perceive are formed by visible light reflected from objects. The color of an object is determined by its reflection spectrum.[55,56] In real scenes, different objects have various reflection spectra in the visible light band, creating colorful landscapes. Likewise, they also have different reflection properties in the NIR light band, which are undetectable to the human naked eye. However, these reflection properties can be detected by the tUCL system, allowing humans to recognize NIR "colors" of these objects under NIR light. To demonstrate the recognition of humans with tUCLs to a reflective image under NIR light, we employed a series of homogeneous reflective mirrors with different reflection spectra to simulate this process (Figure 6A). These reflective mirrors exhibited diverse colors under visible and NIR light, as confirmed by their coordinates on the chromaticity diagram (Figures 6B–6D and S6C–S6E). Interestingly, some reflective mirrors displayed a monotonous color under visible light but exhibited different colors under NIR light (Figures 6B, 6C, and S6C). Some other reflective mirrors displayed different colors under both visible and NIR light (Figures 6D and S6E). This indicates that our tUCL system enables humans to identify various reflection spectra of objects in the NIR-light band, thereby perceiving more abundant color information in the NIR region. Additionally, using the wearable eyeglass system, we could observe colorful letter patterns (Figures 6E and 6F). Some of these patterns appeared black or

Please cite this article in press as: Ma et al., Near-infrared spatiotemporal color vision in humans enabled by upconversion contact lenses, Cell (2025), https://doi.org/10.1016/j.cell.2025.04.019

white under visible light but showed diverse colors under NIR light (Figure 6E), while other patterns displayed vibrant colors under both visible and NIR light (Figure 6F). These findings demonstrate that humans can acquire the ability to recognize colorful reflective images under NIR light through the tUCLs.

DISCUSSION

In this study, we developed soft, wearable, and non-invasive UCLs to extend human vision across multiple NIR spectra, allowing humans to distinguish NIR's temporal, spatial, and color information.

Soft and optically transparent contact lenses based on polymeric materials are widely used to correct the refractive errors of human eyes.[23,33] This provides a wearable solution to achieve human NIR vision. However, integrating nanoparticles into polymeric materials alters their optical properties, posing a challenge in creating high-concentration, optically transparent nanocomposites.[25–27] To address this, we modified UCNPs and screened polymeric materials based on refractive index matching. As a result, we developed NIR-light UCLs with over 90% transparency across most wavelengths at a UCNP mass ratio of 7%. This represents a significant increase compared with the 0.04%–2% mass ratio of UCNPs in some reported transparent nanocomposites.[19,34,40,57] This indicates that we successfully balanced the fusion of UCNPs in the UCLs and their optical properties.

These wearable UCLs can transmit stealthy NIR information without energy support even with closed eyes. Because of the stronger penetration capability of NIR light, the UCLs can be applied not only for night vision but also in foggy or dusty conditions. Although participants wearing UCLs could recognize the temporal information of the flickering NIR light and the direction of NIR light from specific visual quadrants, UCLs cannot achieve fine image perception from an optical principle standpoint, because the upconverted scattered visible light alters the spatial information originally carried by the NIR light before entering the human eye. To overcome this, we designed the wearable eyeglass system to enable participants to distinguish the NIR moving gratings with a spatial resolution threshold of about 65 c/d. This is comparable to the typical spatial resolution threshold (~60 c/d) of human vision,[58,59] suggesting that humans can achieve the NIR vision with normal visual spatial resolution through this method. In the future, to achieve fine NIR vision through UCLs, the UCNP emission process can be designed to ensure that the emitted visible light follows the same path as the incident NIR light, preserving the spatial information carried by the direction of light propagation. For instance, nanoparticles could be engineered to emit light only in the forward direction,[60] or microscale optical fiber channels could be embedded in the UCLs to guide the converted visible light exclusively toward the eye.

Additionally, we can convey multispectral NIR-light information through tUCLs and achieve human NIR color vision. Trichromatic orthogonal UCNPs in these tUCLs allow for the detection of NIR light across three different wavelength regions. Although some studies have reported on multispectral UCNPs, and even their integration with polymers, these works have not truly achieved human NIR color vision.[20,38,61] The practical application of these technologies is limited by factors such as low concentrations of nanoparticle doping and the high-power NIR-light requirements. In contrast, we have overcome these challenges and provided an approach to achieving high-transparency and high-content characteristics through effective optimization of the refractive index of nanoparticles and hydrogels. As such, this work advances the development of trichromatic orthogonal particles for biological visual sensation and recognition. Furthermore, the excitation and emission spectra of these nanomaterials can be adjusted by adding sensitizers and activators, altering core-shell nanostructures and host materials.[62–64] This enables us to detect a wider range of NIR wavelengths through NIR color vision, thereby perceiving more comprehensive NIR information in the future.

Overall, this concept-proving study confirms that human super-vision ability can be achieved by wearable nano-biomaterials and paves the way to numerous applications of human NIR spatiotemporal color vision.

Limitations of the study

In this study, we demonstrated that humans could identify NIR-light information through UCLs at relatively low light intensities, specifically at the LED (Light Emitting Diode) level. However, detecting environmental NIR information in the natural conditions at night without NIR illumination still remains challenging, requiring further advancements in material science and optical design. Through a wearable eyeglass system that does not require battery power, humans can achieve fine NIR vision with normal visual spatial resolution. However, these contact lenses currently cannot achieve fine image perception due to the optical principle limitations. In the future, to achieve fine NIR vision through UCLs, UCNPs need to be designed to emit visible light in the same direction as the incident NIR light, or microscale optical fiber channels embedded in the UCLs are used to guide the emitted light directly to the eye. Additionally, multiplexing visible and infrared information could potentially affect the color constancy of certain objects. Nevertheless, users might adapt and gain integrative perceptions through short-term visual adaptation and learning. Furthermore, the sample size, as well as the sex, racial, and ethnic composition of the participants, may influence the results. Conducting validation studies with a more diverse population could enhance the generalizability of the findings. Although this work has its limitations, it opens the door to a richly informative, colorful NIR world that can be directly perceived by humans.

RESOURCE AVAILABILITY

Lead contact

Further information and requests for resources and reagents should be directed to and will be fulfilled by the lead contact, Tian Xue (xuetian@ustc.edu.cn).

Materials availability

This study did not generate new unique reagents.

Data and code availability

- Raw data from electrophysiological, animal behavioral, human psychophysical experiments, and the analysis of UCL properties have been deposited at Mendeley Data and are publicly available as of the date of publication. Accession numbers are listed in the key resources table.

- This paper does not report original code.
- Any additional information required to reanalyze the data reported in this paper is available from the lead contact upon request.

ACKNOWLEDGMENTS

We thank Dr. Yuao Chen and Xufei Yin from University of Science and Technology of China for helping with optical design of the wearable eyeglass system. This work was funded by the Science and Technology Innovation 2030 Major Program (2021ZD0203100 to Y.M. and 2022ZD0210000 to R.L.); the National Key Research and Development Program of China (2024YFA1803200 to J.M., 2024YFB4707700 to M.Z., and 2024YFB4707700 to J.-N.L.); the Natural Science Foundation (grant no. 32121002, 81925009, 32430046, and 32241010 to T.X.; 32422034, 31900712, and 32271040 to Y.M.; 92368109 and 32471020 to M.Z.; 82495180 to J.M.; 82201230 to R.L.; 12132016 to X. G.; and 32400825 to J.S.); the CAS Project for Young Scientists in Basic Research (YSBR-013 to T.X., YSBR-097 to J.M., and YSBR-041 to R.L.); the Major Scientific and Technological Program of Anhui Province (202303a07020002 to Y.M. and 202303a07020004 to M.Z.); the Anhui Provincial Natural Science Foundation (grant no. 2208085J29 to M.Z.); the Feng Foundation of Biomedical Research to T.X.; and the Human Frontier Science Program (RGY-0090/2014 to G.H. and T.X.). This work has been supported by the New Cornerstone Science Foundation through the New Cornerstone Investigator Program and the XPLORER PRIZE.

AUTHOR CONTRIBUTIONS

Conceptualization, T.X., Y.M., and G.H.; methodology, Y.M., Y.C., S.W., Z.-H.C., Y.Z., L.H., X.Z., F.Y., Y.W., M.Y., Y.Y., F.Z., X.G., G.H., and T.X.; investigation, Y. M., Y.C., S.W., Z.-H.C., Y.Z., L.H., X.Z., F.Y., Y.W., M.Y., Zhanjun Li, K.H., X.F., Zishuo Li, M. Wang, W.L., J.-N.L., L.L., H.Z., M. Wei, Y.S., R.L., M.Z., J.C., J.S., J. M., Y.Y., F.Z., X.G., G.H., and T.X.; writing, Y.M., Y.C., S.W., Z.-H.C., Y.Z., F.Z., X.G., G.H., and T.X.; supervision, T.X.; funding acquisition, Y.M. and T.X.

DECLARATION OF INTERESTS

The authors declare no competing interests.

STAR★METHODS

Detailed methods are provided in the online version of this paper and include the following:

- KEY RESOURCES TABLE
- EXPERIMENTAL MODEL AND STUDY PARTICIPANT DETAILS
  - Human participants
  - Animal
- METHOD DETAILS
  - Synthesis of oleate-free Au/ $NaGdF_4$: Yb^{3+}, Er^{3+} nanoparticles
  - Synthesis of polymers and UCNPs-fused polymer nanocomposites
  - Refractive index measurement of nanoparticles and polymers
  - Characteristics detections of UCLs
  - Synthesis of trichromatic and orthogonal multi-shell lanthanide nanoparticles
  - Spectrum analysis
  - Histology and toxicity test
  - Single-cell electrophysiology (suction pipette recordings)
  - Electroretinography
  - Pupillary light reflex
  - Light-dark box
  - Light-induced fear conditioning
  - Visually evoked potential
  - Optical imaging of intrinsic signals
  - Light-induced conditioned place avoidance
  - NIR temporal and spatial information discrimination of humans through UCLs
  - Human NIR color vision through tUCLs
- QUANTIFICATION AND STATISTICAL ANALYSIS
  - Randomization and blinding
  - Statistics reproducibility
- ADDITIONAL RESOURCES

Received: July 28, 2024
Revised: December 26, 2024
Accepted: April 14, 2025
Published: May 22, 2025

REFERENCES

1. Mandal, M.K. (2003). The Human Visual System and Perception. In Multimedia Signals and Systems (Springer), pp. 33–56. https://doi.org/10.1007/978-1-4615-0265-4_3.
2. Herman, I.P. (2016). Light, Eyes and Vision. In Physics of the Human Body, I.P. Herman, ed. (Springer International Publishing), pp. 731–817. https://doi.org/10.1007/978-3-319-23932-3_11.
3. Schnapf, J.L., Kraft, T.W., Nunn, B.J., and Baylor, D.A. (1988). Spectral sensitivity of primate photoreceptors. Vis. Neurosci. *1*, 255–261. https://doi.org/10.1017/s0952523800001917.
4. Jacobs, G.H. (2012). The Evolution of Vertebrate Color Vision. In Sensing in Nature, C. López-Larrea, ed. (Springer), pp. 156–172.
5. Palczewska, G., Vinberg, F., Stremplewski, P., Bircher, M.P., Salom, D., Komar, K., Zhang, J., Cascella, M., Wojtkowski, M., Kefalov, V.J., et al. (2014). Human infrared vision is triggered by two-photon chromophore isomerization. Proc. Natl. Acad. Sci. USA *111*, E5445–E5454. https://doi.org/10.1073/pnas.1410162111.
6. St George, R.C. (1952). The interplay o light and heat in bleaching rhodopsin. J. Gen. Physiol. *35*, 495–517. https://doi.org/10.1085/jgp.35.3.495.
7. Ala-Laurila, P., Albert, R.J., Saarinen, P., Koskelainen, A., and Donner, K. (2003). The thermal contribution to photoactivation in A2 visual pigments studied by temperature effects on spectral properties. Vis. Neurosci. *20*, 411–419. https://doi.org/10.1017/s0952523803204065.
8. Baylor, D.A., Matthews, G., and Yau, K.W. (1980). Two components of electrical dark noise in toad retinal rod outer segments. J. Physiol. *309*, 591–621. https://doi.org/10.1113/jphysiol.1980.sp013529.
9. Luo, D.G., Yue, W.W.S., Ala-Laurila, P., and Yau, K.W. (2011). Activation of visual pigments by light and heat. Science *332*, 1307–1312. https://doi.org/10.1126/science.1200172.
10. Rao, T., Chen, M., Mu, G., and Tang, X. (2022). Infrared-to-Visible Upconversion Devices. Coatings *12*, 456. https://doi.org/10.3390/coatings12040456.
11. Chen, J., Tao, J., Ban, D., Helander, M.G., Wang, Z., Qiu, J., and Lu, Z. (2012). Hybrid Organic/Inorganic Optical Up-Converter for Pixel-Less Near-Infrared Imaging. Adv. Mater. *24*, 3138–3142. https://doi.org/10.1002/adma.201200587.
12. Kim, D.Y., Song, D.W., Chopra, N., De Somer, P., and So, F. (2010). Organic Infrared Upconversion Device. Adv. Mater. *22*, 2260–2263. https://doi.org/10.1002/adma.200903312.
13. Yu, H., Kim, D., Lee, J., Baek, S., Lee, J., Singh, R., and So, F. (2016). High-gain infrared-to-visible upconversion light-emitting phototransistors. Nat. Photonics *10*, 129–134. https://doi.org/10.1038/nphoton.2015.270.
14. Ma, Y., Bao, J., Zhang, Y., Li, Z., Zhou, X., Wan, C., Huang, L., Zhao, Y., Han, G., and Xue, T. (2019). Mammalian Near-Infrared Image Vision through Injectable and Self-Powered Retinal Nanoantennae. Cell *177*, 243–255.e15. https://doi.org/10.1016/j.cell.2019.01.038.
15. Boye, S.E., Boye, S.L., Lewin, A.S., and Hauswirth, W.W. (2013). A comprehensive review of retinal gene therapy. Mol. Ther. *21*, 509–519. https://doi.org/10.1038/mt.2012.280.
16. Irigoyen, C., Amenabar Alonso, A., Sanchez-Molina, J., Rodríguez-Hidalgo, M., Lara-López, A., and Ruiz-Ederra, J. (2022). Subretinal Injection

Techniques for Retinal Disease: A Review. J. Clin. Med. *11*, 4717. https://doi.org/10.3390/jcm11164717.

17. Malacara, D.; Society of Photo-optical Instrumentation Engineers (2011). Color Vision and Colorimetry: Theory and Applications, Second Edition (SPIE).
18. Vasilopoulou, M., Fakharuddin, A., García de Arquer, F.P., Georgiadou, D. G., Kim, H., Mohd Yusoff, A.R.b., Gao, F., Nazeeruddin, M.K., Bolink, H.J., and Sargent, E.H. (2021). Advances in solution-processed near-infrared light-emitting diodes. Nat. Photonics *15*, 656–669. https://doi.org/10.1038/s41566-021-00855-2.
19. Wang, F., Han, Y., Lim, C.S., Lu, Y., Wang, J., Xu, J., Chen, H., Zhang, C., Hong, M., and Liu, X. (2010). Simultaneous phase and size control of upconversion nanocrystals through lanthanide doping. Nature *463*, 1061–1065. https://doi.org/10.1038/nature08777.
20. Liu, X., Chen, H., Wang, Y., Si, Y., Zhang, H., Li, X., Zhang, Z., Yan, B., Jiang, S., Wang, F., et al. (2021). Near-infrared manipulation of multiple neuronal populations via trichromatic upconversion. Nat. Commun. *12*, 5662. https://doi.org/10.1038/s41467-021-25993-7.
21. Soliman, D. (2016). Augmented microscopy: Development and application of high-resolution optoacoustic and multimodal imaging techniques for label-free biological observation. https://doi.org/10.13140/RG.2.2.24410.03525.
22. Wojtanowski, J., Mierczyk, Z., and Zygmunt, M. (2008). Laser remote sensing of underwater objects. Proc. SPIE. https://doi.org/10.1117/12.799779.
23. Correa, S., Grosskopf, A.K., Lopez Hernandez, H., Chan, D., Yu, A.C., Stapleton, L.M., and Appel, E.A. (2021). Translational Applications of Hydrogels. Chem. Rev. *121*, 11385–11457. https://doi.org/10.1021/acs.chemrev.0c01177.
24. Xu, R., Fang, Y., Zhang, Z., Cao, Y., Yan, Y., Gan, L., Xu, J., and Zhou, G. (2023). Recent Advances in Biodegradable and Biocompatible Synthetic Polymers Used in Skin Wound Healing. Materials (Basel) *16*, 5459. https://doi.org/10.3390/ma16155459.
25. Loste, J., Lopez-Cuesta, J.-M., Billon, L., Garay, H., and Save, M. (2019). Transparent polymer nanocomposites: An overview on their synthesis and advanced properties. Prog. Polym. Sci. *89*, 133–158. https://doi.org/10.1016/j.progpolymsci.2018.10.003.
26. Wang, X., and Cao, Y. (2020). Characterizations of absorption, scattering, and transmission of typical nanoparticles and their suspensions. J. Ind. Eng. Chem. *82*, 324–332. https://doi.org/10.1016/j.jiec.2019.10.030.
27. Demir, M.M., and Wegner, G. (2012). Challenges in the preparation of optical polymer composites with nanosized pigment particles: a review on recent efforts. Macromol. Mater. Eng. *297*, 838–863. https://doi.org/10.1002/mame.201200089.
28. Liu, Y., Wang, D., Shi, J., Peng, Q., and Li, Y. (2013). Magnetic tuning of upconversion luminescence in lanthanide-doped bifunctional nanocrystals. Angew. Chem. Int. Ed. Engl. *52*, 4366–4369. https://doi.org/10.1002/anie.201209884.
29. Zhou, Q.F., Bao, J.C., and Xu, Z. (2002). Shape-controlled synthesis of nanostructured gold by a protection–reduction technique. J. Mater. Chem. *12*, 384–387. https://doi.org/10.1039/b103767f.
30. Shafiqa, A.R., Abdul Aziz, A., and Mehrdel, B. (2018). Nanoparticle Optical Properties: Size Dependence of a Single Gold Spherical Nanoparticle. J. Phys.: Conf. S. *1083*, 012040. https://doi.org/10.1088/1742-6596/1083/1/012040.
31. Bogdan, N., Vetrone, F., Ozin, G.A., and Capobianco, J.A. (2011). Synthesis of ligand-free colloidally stable water dispersible brightly luminescent lanthanide-doped upconverting nanoparticles. Nano Lett. *11*, 835–840. https://doi.org/10.1021/nl1041929.
32. Wichterle, O., and Lím, D. (1960). Hydrophilic Gels for Biological Use. Nature *185*, 117–118. https://doi.org/10.1038/185117a0.
33. Musgrave, C.S.A., and Fang, F. (2019). Contact Lens Materials: A Materials Science Perspective. Materials (Basel) *12*, 261. https://doi.org/10.3390/ma12020261.
34. Na, H., Jeong, J.S., Chang, H.J., Kim, H.Y., Woo, K., Lim, K., Mkhoyan, K. A., and Jang, H.S. (2014). Facile synthesis of intense green light emitting LiGdF4:Yb,Er-based upconversion bipyramidal nanocrystals and their polymer composites. Nanoscale *6*, 7461–7468. https://doi.org/10.1039/c4nr00857j.
35. Park, B.J., Hong, A.R., Park, S., Kyung, K.-U., Lee, K., and Seong Jang, H. (2017). Flexible transparent displays based on core/shell upconversion nanophosphor-incorporated polymer waveguides. Sci. Rep. *7*, 45659. https://doi.org/10.1038/srep45659.
36. Deng, R., Qin, F., Chen, R., Huang, W., Hong, M., and Liu, X. (2015). Temporal full-colour tuning through non-steady-state upconversion. Nat. Nanotechnol. *10*, 237–242. https://doi.org/10.1038/nnano.2014.317.
37. Huang, K., Qiu, H., Zhang, X., Luo, W., Chen, Y., Zhang, J., Chen, Y., Wang, G., and Zheng, K. (2023). Orthogonal Trichromatic Upconversion with High Color Purity in Core-Shell Nanoparticles for a Full-Color Display. Angew. Chem. Int. Ed. Engl. *62*, e202218491. https://doi.org/10.1002/anie.202218491.
38. Hong, A.R., Kyhm, J.-H., Kang, G., and Jang, H.S. (2021). Orthogonal R/G/B Upconversion Luminescence-based Full-Color Tunable Upconversion Nanophosphors for Transparent Displays. Nano Lett. *21*, 4838–4844. https://doi.org/10.1021/acs.nanolett.1c01510.
39. Chai, R., Lian, H., Hou, Z., Zhang, C., Peng, C., and Lin, J. (2010). Preparation and Characterization of Upconversion Luminescent NaYF4:Yb3+, Er3+ (Tm3+)/PMMA Bulk Transparent Nanocomposites Through In Situ Photopolymerization. J. Phys. Chem. C *114*, 610–616. https://doi.org/10.1021/jp909180s.
40. Zhang, W., Jia, H., Ye, H., Dai, T., Yin, X., He, J., Chen, R., Wang, Y., and Pang, X. (2018). Facile Fabrication of Transparent and Upconversion Photoluminescent Nanofiber Mats with Tunable Optical Properties. ACS Omega *3*, 8220–8225. https://doi.org/10.1021/acsomega.8b00648.
41. Sokolov, V.I., Zvyagin, A.V., Igumnov, S.M., Molchanova, S.I., Nazarov, M. M., Nechaev, A.V., Savelyev, A.G., Tyutyunov, A.A., Khaydukov, E.V., and Panchenko, V.Y. (2015). Determination of the refractive index of β-$NaYF_4$/Yb^{3+}/Er^{3+}/Tm^{3+} nanocrystals using spectroscopic refractometry. Opt. Spectrosc. *118*, 609–613. https://doi.org/10.1134/S0030400X15040190.
42. Jacques, S.L. (2013). Optical properties of biological tissues: a review. Phys. Med. Biol. *58*, R37–R61. https://doi.org/10.1088/0031-9155/58/11/R37.
43. Chen, S., Weitemier, A.Z., Zeng, X., He, L., Wang, X., Tao, Y., Huang, A.J. Y., Hashimotodani, Y., Kano, M., Iwasaki, H., et al. (2018). Near-infrared deep brain stimulation via upconversion nanoparticle–mediated optogenetics. Science *359*, 679–684. https://doi.org/10.1126/science.aaq1144.
44. Zhang, X., An, X., Liu, H., Peng, J., Cai, S., Wang, W., Lin, D.-T., and Yang, Y. (2015). The topographical arrangement of cutoff spatial frequencies across lower and upper visual fields in mouse V1. Sci. Rep. *5*, 7734. https://doi.org/10.1038/srep07734.
45. Pearson, R.A., Barber, A.C., Rizzi, M., Hippert, C., Xue, T., West, E.L., Duran, Y., Smith, A.J., Chuang, J.Z., Azam, S.A., et al. (2012). Restoration of vision after transplantation of photoreceptors. Nature *485*, 99–103. https://doi.org/10.1038/nature10997.
46. Schuett, S., Bonhoeffer, T., and Hübener, M. (2002). Mapping retinotopic structure in mouse visual cortex with optical imaging. J. Neurosci. *22*, 6549–6559. https://doi.org/10.1523/JNEUROSCI.22-15-06549.2002.
47. D'hooge, R., and De Deyn, P.P. (2001). Applications of the Morris water maze in the study of learning and memory. Brain Res. Brain Res. Rev. *36*, 60–90. https://doi.org/10.1016/s0165-0173(01)00067-4.
48. Gao, Y.-J., Ren, W.-H., Zhang, Y.-Q., and Zhao, Z.-Q. (2004). Contributions of the anterior cingulate cortex and amygdala to pain-and fear-conditioned place avoidance in rats. Pain *110*, 343–353. https://doi.org/10.1016/j.pain.2004.04.030.
49. Liu, X., Chen, Z.H., Zhang, H., Fan, Y., and Zhang, F. (2021). Independent Luminescent Lifetime and Intensity Tuning of Upconversion Nanoparticles by Gradient Doping for Multiplexed Encoding. Angew. Chem. Int. Ed. Engl. *60*, 7041–7045. https://doi.org/10.1002/anie.202015273.

50. Smith, T., and Guild, J. (1931). The CIE colorimetric standards and their use. Trans. Opt. Soc. *33*, 73–134. https://doi.org/10.1088/1475-4878/33/3/301.

51. Wright, W.D. (1929). A re-determination of the trichromatic coefficients of the spectral colours. Trans. Opt. Soc. *30*, 141–164. https://doi.org/10.1088/1475-4878/30/4/301.

52. Guild, J. (1931). The colorimetric properties of the spectrum. Phil. Trans. R. Soc. Lond. A *230*, 149–187.

53. Wandell, B.A. (1995). Foundations of Vision (Sinauer Associates).

54. Shaw, M., and Fairchild, M. (2002). Evaluating the 1931 CIE color-matching functions. Color Res. Appl. *27*, 316–329. https://doi.org/10.1002/col.10077.

55. Marcus, R.T. (1998). The measurement of color. In Color for Science, Art and Technology (Elsevier), pp. 31–96. https://doi.org/10.1016/S1387-6783(98)80005-6.

56. Klinker, G.J., Shafer, S.A., and Kanade, T. (1987). Using a Color Reflection Model to Separate Highlights from Object Color[1] (Morgan Kaufmann Publishers), p. 614.

57. Chai, R., Lian, H., Cheng, Z., Zhang, C., Hou, Z., Xu, Z., and Lin, J. (2010). Preparation and characterization of upconversion luminescent NaYF4:Yb, Er (Tm)/PS bulk transparent nanocomposites through in situ polymerization. J. Colloid Interface Sci. *345*, 262–268. https://doi.org/10.1016/j.jcis.2010.01.082.

58. Campbell, F.W., and Green, D.G. (1965). Optical and retinal factors affecting visual resolution. J. Physiol. *181*, 576–593. https://doi.org/10.1113/jphysiol.1965.sp007784.

59. Varadharajan, L.S. (2014). Spatial Vision and Pattern Perception. In Handbook of Visual Display Technology, J. Chen, W. Cranton, and M. Fihn, eds. (Springer Berlin Heidelberg), pp. 1–9.

60. Rosemann, N.W., Eußner, J.P., Beyer, A., Koch, S.W., Volz, K., Dehnen, S., and Chatterjee, S. (2016). A highly efficient directional molecular white-light emitter driven by a continuous-wave laser diode. Science *352*, 1301–1304. https://doi.org/10.1126/science.aaf6138.

61. Lee, G., Mun, J., Choi, H., Han, S., and Hahn, S.K. (2021). Multispectral upconversion nanoparticles for near infrared encoding of wearable devices. RSC Adv. *11*, 21897–21903. https://doi.org/10.1039/d1ra03572j.

62. Li, X., Zhang, F., and Zhao, D. (2013). Highly efficient lanthanide upconverting nanomaterials: Progresses and challenges. Nano Today *8*, 643–676. https://doi.org/10.1016/j.nantod.2013.11.003.

63. Cheng, X., Zhou, J., Yue, J., Wei, Y., Gao, C., Xie, X., and Huang, L. (2022). Recent Development in Sensitizers for Lanthanide-Doped Upconversion Luminescence. Chem. Rev. *122*, 15998–16050. https://doi.org/10.1021/acs.chemrev.1c00772.

64. Li, X., Zhang, F., and Zhao, D. (2015). Lab on upconversion nanoparticles: optical properties and applications engineering via designed nanostructure. Chem. Soc. Rev. *44*, 1346–1378. https://doi.org/10.1039/c4cs00163j.

65. Xue, T., Do, M.T.H., Riccio, A., Jiang, Z., Hsieh, J., Wang, H.C., Merbs, S. L., Welsbie, D.S., Yoshioka, T., Weissgerber, P., et al. (2011). Melanopsin signalling in mammalian iris and retina. Nature *479*, 67–73. https://doi.org/10.1038/nature10567.

66. Stockman, A., and Sharpe, L.T. (2000). The spectral sensitivities of the middle- and long-wavelength-sensitive cones derived from measurements in observers of known genotype. Vision Res. *40*, 1711–1737. https://doi.org/10.1016/s0042-6989(00)00021-3.

67. Lovetskiy, K.P., Sevastianov, L.A., and Nikolaev, N.E. (2018). Numerical modeling of color perception of optical radiation. Math. Model. Geom. *6*, 21–36. https://doi.org/10.26456/mmg/2018-612.

Please cite this article in press as: Ma et al., Near-infrared spatiotemporal color vision in humans enabled by upconversion contact lenses, Cell (2025), https://doi.org/10.1016/j.cell.2025.04.019

STAR★METHODS

KEY RESOURCES TABLE

REAGENT or RESOURCE	SOURCE	IDENTIFIER
Antibodies		
Anti Iba1, Rabbit	Wako Pure Chemical Corporation	Cat# 019-19741; RRID: AB_839504
Alexa Fluor 568 goat anti-rabbit IgG (H+L)	Thermo Fisher Scientific	Cat# A-21206; RRID: AB_2535792
Chemicals, peptides, and recombinant proteins		
Isoflurane	RWD	R510-22-10
4% paraformaldehyde	Servicebio	G1101
PBS	Servicebio	G4202
DAPI Stain Solution	Sangon Biotech	E607303-0020
Optimal Cutting temperature (O.C.T) Compound	Sakura	Cat# 4583
Vitamins	Sigma-Aldrich	Cat# M6895
Non-essential Amino Acid Solution	Sigma-Aldrich	Cat# M7145
$GdCl_3{\cdot}6H_2O$	Beijing HwrkChemical Technology Co., Ltd	HWG13063
$YCl_3{\cdot}6H_2O$	Beijing HwrkChemical Technology Co., Ltd	HWG00637
$ErCl_3{\cdot}6H_2O$	Beijing HwrkChemical Technology Co., Ltd	HWG00629
$YbCl_3{\cdot}6H_2O$	Beijing HwrkChemical Technology Co., Ltd	HWG00635
$TmCl_3{\cdot}6H_2O$	Beijing HwrkChemical Technology Co., Ltd	HWG00646
$NdCl_3{\cdot}6H_2O$	Beijing HwrkChemical Technology Co., Ltd	HWG13451
Y_2O_3	Beijing HwrkChemical Technology Co., Ltd	HWG61615
Yb_2O_3	Beijing HwrkChemical Technology Co., Ltd	HWG13421
Er_2O_3	Beijing HwrkChemical Technology Co., Ltd	HWG61491
Tm_2O_3	Beijing HwrkChemical Technology Co., Ltd	HWG11605
Nd_2O_3	Beijing HwrkChemical Technology Co., Ltd	HWG00534
Gd_2O_3	Beijing HwrkChemical Technology Co., Ltd	HWG61493
Sodium trifluoroacetate, Na-TFA	Beijing HwrkChemical Technology Co., Ltd	Beijing HwrkChemical Technology Co., Ltd
Oleic acid, OA	Sigma-Aldrich	364525
1-Octadecene, ODE	Sigma-Aldrich	O806
Trifluoroacetic acid, TFA	Sinopharm Chemical Reagent Co., Ltd.	80134716
Methanol anhydrous, CH_3OH	Sinopharm Chemical Reagent Co., Ltd.	80080418
Ethanol absolute	Sinopharm Chemical Reagent Co., Ltd.	10009218
Cyclohexane	Sinopharm Chemical Reagent Co., Ltd.	80039708
Sodium hydroxide, NaOH	Sinopharm Chemical Reagent Co., Ltd.	10019718
Ammonium fluoride, NH_4F	Sinopharm Chemical Reagent Co., Ltd.	10002008
Polyvinylpyrrolidone, PVP	Sigma-Aldrich	CAS:9003-39-8
Tetraethylene glycol diacrylate, TEGDA	Sigma-Aldrich	CAS:17831-71-9
Azobisisobutyronitrile, AIBN	Aladdin	CAS:78-67-1
PDMS	Dow Corning GmbH, USA	Sylgard 184
3-(methacryloyloxy) propyltris (trimethylsiloxy) silane (TRIS)	Aladdin	CAS: 5356-84-3
1-Vinyl-2-pyrrolidinone, NVP	Aladdin	CAS:88-12-0
Methacrylic acid, MAA	Sigma-Aldrich	CAS:79-41-4
Poly (ethylene glycol) methacrylate, PEGMA	Aladdin	CAS:25736-86-1
N,N-Dimethylacrylamide, DMA	Aladdin	CAS:2680-03-7
2-Hydroxyethyl methacrylate, HEMA	Aladdin	CAS:868-77-9
Acrylamide	Aladdin	CAS:79-06-1
N, N-dimethylacrylamide,DMAA	Sigma-Aldrich	CAS:2680-03-7

(*Continued on next page*)

Please cite this article in press as: Ma et al., Near-infrared spatiotemporal color vision in humans enabled by upconversion contact lenses, Cell (2025), https://doi.org/10.1016/j.cell.2025.04.019

Continued

REAGENT or RESOURCE	SOURCE	IDENTIFIER
Dimethyl sulfoxide, DMSO	Sigma-Aldrich	CAS:67-68-5
PVA nanofillers	Aladdin	P105126
PI-184	Sinopharm Chemical Reagent Co., Ltd.	CAS:947-19-3
2-Hydroxy-2-methylpropiophenone	Aladdin	CAS:7473-98-5
Ethylene glycol dimethacrylate, EGDMA	Aladdin	CAS:97-90-5
1-Hexanol	Sinopharm Chemical Reagent Co., Ltd.	CAS:111-27-3
Contact lens mold	Qingdao Chuangxing Science and Technology Co., Ltd.	N/A
Critical commercial assays		
HE staining	Servicebio Co., Ltd	N/A
TUNEL BrightGreen Apoptosis Detection Kit	Vazyme Biotech Co., Ltd	A112-03
Deposited data		
Raw data from electrophysiological, animal behavioral, human psychophysical experiments, and the analysis of UCL properties	Mendeley Data	Mendeley Data: https://doi.org/10.17632/5cwgxpk3pd.1
Experimental models: Organisms/strains		
Mouse: C57BL/6J, 8 weeks	SPF (Beijing) Experimental Animal Science and Technology Co., Ltd.	N/A
Software and algorithms		
ImageJ	National Institutes of Health (NIH), USA	https://imagej.nih.gov/ij/download.html
Origin 8.0	OriginLab	https://www.originlab.com/
MATLAB	MathWorks	https://www.mathworks.com/products/matlab.html
LabVIEW	National Instrument	http://www.ni.com/en-us/shop/labview/select-edition.html; RRID: SCR_014325
Other		
FLUOVIEW FV3000	Olympus	https://www.olympus-global.com/news/2016/nr160405fv3000e.html
Photometer	Newport	1936-R
Spectrometer	Avantes	ULS2048
Spectrum-color-luminance meter	EVERFINE Corporation	SRC-200S

EXPERIMENTAL MODEL AND STUDY PARTICIPANT DETAILS

Human participants

Participants (18-40 years old) with normal vision and color perception participated in the human NIR vision experiments. This study was conducted in accordance with the ethical guidelines of the First Affiliated Hospital of the University of Science and Technology of China, and all participants signed the informed consent to participate in this study (medical ethics approval number: 2024KY134). The clinical trial was registered and approved on the Chinese Clinical Trial Registry website (registered website: http://www.chictr.org.cn, registration number: ChiCTR2400082802). The sample size of participants for this study was not predetermined using statistical methods. The number of participants in each experiment was consistent with common sample sizes in similar experimental designs within the field. Participants were randomly assigned to different experimental groups. For the tests of visual sensitivity, temporal coding, and pattern vision of humans through UCL, 5 healthy individuals (3 males and 2 females) were recruited, with ages of 27.8 (SD±5.59) years. For the color matching experiment of humans through tUCL, 5 healthy individuals (3 males and 2 females) were recruited, with ages of 22.8 (SD±1.48) years. For the tests of NIR color information discrimination of humans, 5 healthy individuals (3 males and 2 females) were recruited, with ages of 26.6 (SD±3.05) years. All the participants were of East Asian ancestry, of Asian race, and of Han Chinese ethnicity.

Please cite this article in press as: Ma et al., Near-infrared spatiotemporal color vision in humans enabled by upconversion contact lenses, Cell (2025), https://doi.org/10.1016/j.cell.2025.04.019

Animal

The experimental procedures on animals followed the guidelines of the Animal Care and Use Committee at the University of Science and Technology of China. All mice were housed under a 12 h/12 h light/dark cycle and at an ambient temperature of 20-24°C. C57/BL6J mice were purchased from SPF (Beijing) Experimental Animal Science and Technology Co., Ltd. Male mice were used in all experiments.

METHOD DETAILS

Synthesis of oleate-free Au/ $NaGdF_4$: Yb^{3+}, Er^{3+} nanoparticles

$NaGdF_4$: Yb^{3+}, Er^{3+} upconversion nanoparticles (UCNPs) were synthesized by a high-temperature thermal decomposition method as previously reported.[28] These $NaGdF_4$: Yb^{3+}, Er^{3+} nanoparticles were dispersed in DI water and the 2 mL 2.4 mM ligand-linkage polyvinylpyrrolidone (PVP), as well as 20 μL 10 mM chloroauric acid solution were successively added. After stirring for 15 min at 25 °C, 900 μL 100 mM reducing agent of ascorbic acid were dipped. Keeping stirring and reaction for 30 min, Au could load on the surface of UCNPs. The modified nanoparticles were then centrifuged and washed by deionized (DI) water for several times to obtain the purified Au/ $NaGdF_4$: Yb^{3+}, Er^{3+} nanoparticles.[29] To enhance the dispersion of Au/ $NaGdF_4$: Yb^{3+}, Er^{3+} UCNPs in contact lenses and remove oleic acid molecules, a modification process was carried out.[31] First, 50 mg of the nanofillers were dispersed in 10 mL of DI water. Next, 50 μL of 1 M HCl solution was added to the mixture. The suspension was then magnetically stirred for 3 h, followed by multiple rounds of centrifugation and washing. The nano-morphologies of UCNPs were observed by field emission scanning electron microscopy (SEM, Gemini 500, Carl Zeiss Jena, Germany) at an acceleration voltage of 3 kV. A Nicolet Model 759 Fourier transform infrared (FT-IR) spectrometer was applied to characterize the infrared (IR) spectrum of oleate-free UCNPs in the full range of 1000-3500 cm^{-1}.

Synthesis of polymers and UCNPs-fused polymer nanocomposites

Polymethyl methacrylate (PMMA) polymer

A mixture was prepared by combining 200 μL of methyl methacrylate (MMA), 20 μL of 2-hydroxyethyl acrylate (HEA), and 20 μL of tetra (ethylene glycol) diacrylate (TEGDA). Subsequently, 5 mg of azobisisobutyronitrile (AIBN) was introduced as the initiator, and the resulting mixture was subjected to argon bubbling for 5 min. Then the viscous liquid was injected into the Si wafer. The Si wafer was transferred to an oil bath and incubated at 70 °C for 3 h. The solid phase was cooled down to room temperature to obtain the PMMA polymer. Consequently, the PMMA polymer was put in a vacuum oven (0.34 bar, 80 °C) for overnight to remove organic solvent residues, and kept in saline solution before use.

Polydimethylsiloxane (PDMS) polymer and OA-UCNPs-fused PDMS contact lens

OA-UCNPs were firstly totally dispersed into ethanol by ultrasonic treatment for 5 min. Then, 1 g PDMS precursor (Sylgard 184, Dow Corning GmbH, USA) was added, and the mixture was stirred for a period. After cooling down, 0.1 g curing agent was further added and mixed. Put the mixture in a vacuum oven to remove all the air bubbles. Finally, the solution was poured onto the Si wafer or the mold of the contact lens (Qingdao Chuangxing Science and Technology Co., Ltd.) and cured at 90 °C for 10 min. If the sole objective was to synthesize PDMS polymer, the steps involving OA-UCNP fusion could be omitted.

Silicone hydrogel-1 polymer

0.021 g 2-hydroxy-2-methylpropiophenone (Aladdin) and 0.067 g ethylene glycol dimethacrylate (EGDMA, Aladdin) were first added to 1.07 g 1-hexanol (Sinopharm Chemical Reagent Co., Ltd) in a beaker. Then, 5 g 3-(methacryloyloxy) propyltris (trimethylsiloxy) silane (TRIS, Aladdin), 3 g 1-vinyl-2-pyrrolidinone (NVP, Aladdin), 0.5 g methacrylic acid (MAA, Sigma-Aldrich) and 1 g poly (ethylene glycol) (PEGMA, Aladdin) were also added and they were stirred in dark environment for 6 h. The mixture was then transferred onto the Si wafer and cured under UV light (365 nm) for 1 h. The resultant composite was purified in water/ethanol solution (vol/vol=1:1) and heated at 50 °C for 12 h to remove all the unreacted monomers.

Silicone hydrogel-2 polymer and UCNPs-fused silicone hydrogel-2 contact lens

3-(methacryloyloxy) propyltris (trimethylsiloxy) silane (TRIS, Aladdin), N, N-dimethylacrylamide (DMA, Aladdin), 1-vinyl-2-pyrrolidinone (NVP, Aladdin), 2-hydroxyethyl methacrylate (HEMA, Aladdin), ethylene glycol dimethacrylate (EGDMA, Aladdin) and PI-184 (Sinopharm chemical Reagent Co., Ltd) with the mass ratio of 40%, 30%, 17%, 12%, 0.6% and 0.4% were mixed for 5 h under dark environment. Then, UCNPs were introduced into the solution by ultrasonic treatment for 5 min, and the mixture was added onto the glass mold under N_2 atmosphere and cured under UV light (365 nm) for 15 min. Finally, the film was purified by ethanol/water solution (vol:vol=1:1) at 50 °C for 24 h.

pHEMA-1 polymer and UCNPs or OA-UCNPs-fused pHEMA-1 contact lens

2-hydroxyethyl methacrylate, 2-hydroxy-2-methylpropiophenone and ethylene glycol dimethacrylate were purchased from Aladdin and used without further purification. Firstly, 0.085 g ethylene glycol dimethacrylate was dipped into 4 mL 2-hydroxyethyl methacrylate. Then, 3 mL DI water and 0.085 g 2-hydroxy-2-methylpropiophenone were stepwise added. The solution was stirred for 30 min under the dark environment and finally the monomer suspension was sealed to avoid visible light.

UCNPs or OA-UCNPs were added into the above monomer solution with sonification treatment. Then, dipping them into the Si wafer or the mold of the contact lens and illuminated by UV light (365 nm) for 20 min to catalyze the reaction. The film or contact

lens was further peeled from the Si wafer or the mold and washed with DI water/ethanol solution (with a volume ratio of 1:1) at 50 °C for 10 h to remove the unreactive monomers. If the sole objective was to synthesize pHEMA-1 polymer, the steps involving UCNP or OA-UCNP fusion could be omitted.

pHEMA-2 polymer and UCNPs-fused pHEMA-2 contact lens

2-hydroxyethyl methacrylate (HEMA, Aladdin), cross-linker ethylene glycol dimethacrylate (EGDMA, Aladdin), and photo-initiator 2-hydroxy-2-methylpropiophenone (Aladdin) were mixed in a volume ratio of 95:4:1 and stirred magnetically for 0.5 h. Then, the above solution and UCNPs were mixed and sonicated for 5 min, and dripped onto the Si wafer or the mold of the contact lens and cured under UV light (365 nm) for 10 min. Finally, the film or contact lens was further peeled from the Si wafer or the mold and washed with DI water/ethanol solution (with a volume ratio of 1:1) at 50 °C for 12 h to remove all the unreacted monomers. If the sole objective was to synthesize pHEMA-2 polymer, the steps involving UCNP fusion could be omitted.

PVA hydrogel polymer

4 mL dimethyl sulfoxide (DMSO, Sigma Aldrich) and 1 mL DI water were first mixed. Then, 1.2 g PVA nanofillers (Aladdin, 1799) were added and stirred at 90 °C for 5 h to obtain a transparent PVA solution. The solution was dripped onto the Si wafer or the mold of the contact lens and frozen at -25 °C for 12 h. Finally, the film or contact lens was rinsed in DI water to remove extra DMSO at 37 °C. If the sole objective was to synthesize PVA hydrogel, the steps involving UCNPs fusion could be omitted.

PAA hydrogel polymer and UCNPs-fused PAA contact lens

2.3 g acrylamide (Aladdin) was dissolved into 10 mL DI water. Then, 17 mg N, N-dimethylacrylamide (DMAA, Sigma-Aldrich) and 37.5 μL 0.8 mol/L 2, 2'-Azobis(2-methylpropionamidine) dihydrochloride (Aladdin) and UCNPs were added to the solution. After all the chemical agents were dissolved, the mixture was poured onto the Si wafer and maintained at 50 °C for 8 h. Finally, the film was placed into the water to remove all the unreacted agents.

Refractive index measurement of nanoparticles and polymers

The refractive index of nanoparticles and polymers was measured by Abbe refractometer (WAY-2WAJ, Hangzhou Jingfei Instrument Technology Co., Ltd.). A method for measuring the refractive index n of nanoparticles in the visible ranges is based on comparing the refractive index $n_{colloid}$ of a colloid solution of nanoparticles in several solvents with refractive indices $n_{solvent}$ of corresponding pure solvents.[41] UCNPs (oleate-free) were dispersed within zinc bromide solutions of varying mass concentrations (0.2682 g/mL, 0.6705 g/mL, 0.8940 g/mL, 1.1846 g/mL, 1.5645 g/mL), corresponding to distinct refractive indices (1.3725, 1.4195, 1.4440, 1.4874, 1.5322, respectively). This process resulted in the formation of stable colloidal solutions with a final nanoparticle mass fraction of 12%. Then, the refractive indices of these colloidal solutions and polymers were measured. For oleate-capped UCNPs (OA-UCNPs), non-polar organic solvents including hexane, cyclohexane, decalin (a mixture of cis- and trans-decalin), decalin + 10% adamantane, benzyl-methacrylate, were used as the solvents.[41] The refractive indices of these solvents and colloidal solutions were measured. All refractive index measurements were conducted at a room temperature of 20 °C.

Characteristics detections of UCLs

To measure the transmittance of UCLs, we used a spectrophotometer (Shimadzu UV-1800) to acquire this parameter of UCLs. The scan range of the spectrum was 380-700 nm. The nano-morphologies of UCLs were observed by field emission scanning electron microscopy (SEM, Gemini 500, Carl Zeiss Jena, Germany) at an acceleration voltage of 3 kV. The zeta potential and hydrodynamic size distribution of UCNPs in the mixed solution before curing were measured by Zetasizer Nano ZS90 (Malvern Panalytical, England). The hydrophily of UCLs was measured by a Water Drop Angle Test Instrument (CHD-JCJ180A-1). To determine the moisture content of UCLs, the surface water of contact lenses was first removed and their mass was measured as m_1. Next, the lenses were dried completely in a 50 °C oven for 48 h and their mass was measured again as m_2. The water content of contact lenses was then calculated as $(m_1-m_2)/m_1$. The rheological properties of UCNPs-pHEMA contact lenses as well as commercial contact lenses were tested by a commercial rheometer (Physica MCR 301, Anton Paar Co., Austria) in frequency sweep test mode. The strain was set at 0.1% while the shear frequency was varied from 0.1 Hz to 100 Hz at room temperature. Pre-shearing was also carried out before all the rheological tests. The stability of the rheological response was assessed by changing the shear frequency from 0.1 Hz to 10 Hz with the strain of 0.1%. Tensile tests were carried out by a dynamic mechanical analyzer (DMA, typed Electro-Force 3200 from TA. Instruments Inc.). The tensile rate was kept at 0.005 s^{-1}. Data were analyzed with OriginPro 2018 (Origin Lab Corp.).

Synthesis of trichromatic and orthogonal multi-shell lanthanide nanoparticles

The synthesis of β-$NaErF_4$ core nanoparticles was similar to the traditional thermolysis method with several modifications. In brief, 1 mmol Erbium chloride ($ErCl_3{\cdot}6H_2O$) was mixed with 6 mL OA and 15 mL ODE in a three-neck 100 mL round-bottom flask with Schlenk lines and a thermocouple temperature sensor. The mixture was then heated to 140°C and maintained at this temperature for 60 minutes to remove the remaining water. When the mixture was cooled down to room temperature, 2.5 mmol NaOH (100 mg) dissolved in 5 mL CH_3OH was added and stirred for 30 min. Then, the mixture was heated to 100 °C to remove methanol under vacuum before cooling down to room temperature. After that, 4 mmol NH_4F (148 mg) dissolved in 10 mL CH_3OH was added, and the mixture was stirred for another 30 min and then heated to 100 °C to remove methanol and residual water under the vacuum. Afterward, the clear solution was heated to 300 °C for 60 min under a gentle Ar flow (heating rate 10 °C/min). When the reaction system was cooled down to room temperature, the synthesized nanoparticles were centrifuged and washed three times with

cyclohexane/ethanol (with a volume ratio of 1:1) and finally dispersed in 10 mL cyclohexane for further use. Here, we defined normalized molar as-synthesized core and core-multi shell nanoparticles according to molar lanthanide chloride used in the core. The concentration of the synthesized nanoparticles in cyclohexane was defined as 0.1 mmol/mL $NaErF_4$ (Er core) in this work. The size and distribution were depicted in Figure S4A.

The synthetic method of Ln-TFA (lanthanide trifluoroacetate) was proceeded by mixing lanthanide oxides and TFA. NaErF4@$NaYF_4$ core-shell nanoparticles were synthesized through the conventional epitaxial growth method for various lanthanide core-shell nanoparticles. The former $NaErF_4$ nanoparticles (0.2 mmol in total) in cyclohexane were used as seeds. 0.4 mmol Na-TFA and 0.4 mmol Y-TFA were used as the precursors for the epitaxial growth of $NaYF_4$ shell. By addition of 3.2 mL OA and 4.8 mL ODE, the mixture was then heated to 100 °C to remove cyclohexane and other residues under vacuum. After that, the mixture was heated to 300 °C for 60 min under a gentle Ar flow (heating rate 10 °C/min). When the reaction system was cooled down to room temperature, the synthesized nanoparticles were then centrifuged and washed three times with cyclohexane/ethanol (1:1) and finally dispersed in 2 mL cyclohexane for further use (Er@Y). The size and distribution were depicted in Figure S4B. By changing the amount of precursors used in each step, other multilayer core-shell nanoparticles could be synthesized. Figure S4C, 0.6 mmol Na-TFA (81.6 mg), 0.012 mmol Er-TFA (145.0 mg), 0.48 mmol Y-TFA (205.3 mg) and 0.108 mmol Yb-TFA (55.4 mg). Figure S4D, 0.4 mmol Na-TFA (54.4 mg), 0.08 mmol Yb-TFA (41.0 mg) and 0.32 mmol Y-TFA (136.9 mg). Figure S4E, Nd-TFA (145.0 mg), 0.18 mmol Y-TFA (77.0 mg) and 0.12 mmol Yb-TFA (61.5 mg). Figure S4F, 0.6 mmol Na-TFA (81.6 mg) and 0.6 mmol Y-TFA (256.8 mg). Figure S4G, 0.8 mmol Na-TFA (108.8 mg), 0.64 mmol Yb-TFA (327.7 mg), 0.008 mmol Tm-TFA (4.0 mg) and 0.152 mmol Y-TFA (65.0 mg). Figure S4H, 1 mmol Na-TFA (136 mg) and 1 mmol Y-TFA (428 mg). The oleate ligands from trichromatic UCNPs were removed and trichromatic UCLs were obtained using the aforementioned method.

Spectrum analysis

The excitation and emission spectra were obtained through a two-photon microscope (SP8, Leica, Germany). The excitation spectrum was measured by varying the excitation wavelength from 680 nm to 1080 nm and recording the emission intensity at the peak wavelength. The emission spectrum was obtained by irradiating the sample with CW lasers at 980 nm, 808 nm, and 1532 nm, and recording the emission intensity in the range of 380 nm to 700 nm. The wavelength step was 5 nm. For excitation spectrum measurement of trichromatic UCNPs, we used a UV-Vis-NIF Spectrometer (SolidSpec-3700DUV) to acquire the absorbance of solid nanoparticles illuminated by 750-1600 nm light.

Histology and toxicity test

To evaluate potential ocular toxicity, the UCLs were attached to the mouse corneas and maintained for 6 hours. Mice were anesthetized with isoflurane using pure oxygen as the carrier gas. During anesthesia induction, the oxygen flow rate was set at 1 L/min with an isoflurane concentration of 3%. Once anesthesia was achieved, the isoflurane concentration was reduced and maintained at 1% throughout the procedure. For long-term toxicity tests, the UCLs were attached to the corneas of mice anesthetized with isoflurane. The experiments were conducted for 6 hours per day, with durations of 3, 7, or 14 consecutive days. After this, the corneas and retinae were fixed and hematoxylin-eosin (HE) staining was performed. Corneal thickness and the number of retinal cell layers served as parameters for assessing the degree of ocular damage. The thickness and cell layers were counted at 5 different locations on each corneal and retinal slice, and this process was repeated on 5 randomly selected slices from each eye. Results were then averaged to obtain a comprehensive assessment of potential toxicity. Meanwhile, detection of cell apoptosis using TUNEL apoptosis detection kit (Terminal deoxynucleotidyl transferase dUTP nick end labeling, Vazyme Biotech Co., Ltd-A113) and immune reactions using Iba1 (ionized calcium-binding adapter molecule 1, one marker protein of microglia) staining assay were conducted as according to the previous report.[14]

Single-cell electrophysiology (suction pipette recordings)

For rod suction pipette recordings, C57 wild-type mice were dark-adapted for at least 3 hours. Mice's eyes were enucleated after euthanasia with tribromoethanol (Avertin, 450 mg/kg, Sigma-Aldrich). The retina was carefully isolated from the eye and flat-mounted onto the trimmed UCLs (diameter ~5 mm) in the recording chamber. Recordings were carried out on an Olympus upright infrared-DIC microscope. The bath solution was Ames medium (in mM): 120 NaCl, 22.6 $NaHCO_3$, 3.1 KCl, 0.5 KH_2PO_4, 1.5 $CaCl_2$, 1.2 $MgSO_4$, 6 Glucose, equilibrated with 5% CO_2 / 95% O_2 and heated to 32-34 °C (Warner Instruments Corp, TC-3448). The outer segment of a rod was gently sucked into a ~1.6 μm diameter glass pipette filled with modified Ames solution (in mM): 135 NaCl, 10 mM HEPES, 3.1 KCl, 0.5 KH_2PO_4, 1.5 $CaCl_2$, 1.2 $MgSO_4$, 6 Glucose, pH adjusted to 7.4 by NaOH. Stimulation light was applied through the imaging objective. The 535-nm light was from a filter block in front of a white light LED. Infrared light was generated by the 980-nm laser. A series of photoreceptor responses were induced by 15-ms flashes of 535 nm or 980 nm at different intensities. Data were lowpass filtered at 50 Hz and sampled at 25 kHz by Axon 700B Amplifier and Digital 1440A interface.

Electroretinography

Pupils of C57 wild-type mice were dilated with atropine (100 μg/mL, Sigma-Aldrich) and then mice were anesthetized by Avertin (450 mg/kg, Sigma-Aldrich). During the experiment, the anesthetized animal was kept on a warming blanket and its eyes were kept wet to avoid cataracts. Mice were placed into a Faraday cage and the tip of a silver recording electrode was put tightly against

Please cite this article in press as: Ma et al., Near-infrared spatiotemporal color vision in humans enabled by upconversion contact lenses, Cell (2025), https://doi.org/10.1016/j.cell.2025.04.019

the center of the cornea, while a UCL was placed on the cornea. A ground electrode was inserted into the subcutaneous space of the tail and a reference electrode was inserted into the subcutaneous space of the head. A 535-nm LED light or a 980-nm laser beam was placed in front of the pupil for stimulation. A series of ERG responses were induced by 20-ms flashes of 535 nm or 980 nm at different intensities. Data acquisition were carried out by a differential amplifier (AM-SYSTEM INC) and Digital 1440A (Axon CNS). Data were lowpass filtered at 50 Hz and sampled at 5 kHz, and amplitudes of b-waves in ERG traces were used to characterize the light-induced retinal responses.

Pupillary light reflex

C57 wild-type mice were anesthetized with an intraperitoneal injection of Avertin (450 mg/kg). A UCL was placed onto one eye of each mouse, and then mice were carefully monocular sutured with the surgical needle. A small amount of 1% Penicillin/Streptomycin solution (Sangon-BS732) in PBS was applied to mice's eyes before and after the suture to prevent infection. At the same time, a patch of skin overlying the skull was excised, and four bone screws were threaded into the skull, with care taken to prevent any damage to the brain. These screws were covered with dental cement, and served as the foundation for a stainless-steel post. Under anesthesia, mice's eyes were kept wet with eye gel to avoid cataracts.

After two days of recovery, mice were head-fixed for pupillometry of long-duration measurements.[65] For pupillometry, the stainless-steel post was clamped to immobilize the mouse head within an acrylic holder. To measure the PLR of an unsutured eye simultaneously, we built a pupillometer with a miniature, infrared CCD camera and 850 nm LED light for video recording via a ganzfeld sphere. A 535-nm or 980-nm LED was placed close to the sutured eye (1 mm distance) for stimulation. Videos for contralateral eyes were digitized and recorded at a frame rate of 5 Hz. Videos were analyzed with XCAP-Ltd V3.x. The maximum pupil constriction of the unsutured eye during the 40 s light stimulation was measured. The pupil area percentage was calculated as the ratio between the area at the maximum constriction and the area at the beginning of light stimulation.

Light-dark box

Before the test, C57 wild-type mice were anesthetized and binocular sutured with the UCLs inside. A small amount of 1% Penicillin/Streptomycin solution (Sangon-BS732) in PBS was applied to mice's eyes before and after suturing to prevent infection. Under anesthesia, mice's eyes were kept wet with eye gel to avoid cataracts. After two days of recovery, animals were introduced to the custom-made light and dark double box measuring 26 cm (length) $\times$ 13 cm (width) $\times$ 13 cm (height). On each of the three sides of the light box, 75 LEDs emitting at 980 nm (5 Watts) and 75 LEDs emitting at 535 nm (1 Watt), arranged in a 5 $\times$ 5 LED array, were evenly distributed for light stimulation. A series of light stimulations in the order of 5 min in the dark, 5 min in 980-nm light, and 5 min in 535-nm light was programmed. All these experiments were carried out in the dark environment and videos were acquired by an infrared camera and a custom-made software. Time spent in the dark box and time spent in the light box in 5 minutes was measured for the calculation of the preference index for the dark box.

Light-induced fear conditioning

C57 wild-type mice were placed in the 13 cm $\times$ 13 cm $\times$ 13 cm transparent custom-made fear conditioning box. On the surround of four sides of the box, 100 535-nm LEDs or 980-nm LEDs (5 $\times$ 5 LED array on each side) were evenly placed for light stimulation. The training protocol consisted of a 5-min adaptation and a 20-s 535-nm light as the conditioned stimulus (CS) followed by a 2-s electrical foot shock as the unconditioned stimulus (US). Paired CS and US were repeated 6 times at 2-min interval. After training, mice were anesthetized and binocular sutured with the UCLs inside. A small amount of 1% Penicillin/Streptomycin solution (Sangon-BS732) in PBS was applied to mice's eyes before and after suturing to prevent infection. After two days of recovery, a test protocol, that resembled the training protocol but without unconditioned stimulus (US), was used to test mice's freezing time rate in which 2 times 20-s 535-nm light and 2 times 980-nm light randomly as conditioned stimulus (CS). A custom-made software was used to control LED light and electrical shock. Freezing time ratios of Pre-CS (20 s before conditioned stimulus) and CS (40 s, total time of the 2 times 980-nm or 535-nm conditioned stimulus) were analyzed to compare the effect of light-induced freezing.

Visually evoked potential

VEP was carried out as described in the previous report.[14] In short words, a recording glass pipette with the silver electrode in was inserted into right/left primary visual cortex of anesthetized mice and targeted to the following coordinates (relative to bregma): 1-(2.15, -2.95, -0.5), 2-(2.75, -2.95, -0.5), 3-(2.0, -3.28, -0.4), 4-(2.75, -3.28, -0.4) mm. A ground electrode was inserted into the subcutaneous space of the tail and a reference electrode was inserted into the subcutaneous space of the head. While a UCL was placed on the cornea of one eye which was illuminated by 100-ms 980-nm light or 535-nm light, VEP signals of the contralateral exposed primary visual cortex were recorded. The signals were lowpass filtered at 50 Hz and sampled at 5 kHz by a differential amplifier (AM-SYSTEM INC) and digitized by Digital 1440A (Axon CNS).

Optical imaging of intrinsic signals

Surgical preparation, visual stimulation, optical imaging of intrinsic signals, and data analysis were carried out as described previously.[44,45] Mice were anesthetized with isoflurane in an airtight jar supplemented by an intramuscular injection of chlorprothixene (10 mg/kg i.m.). And then, the mice were quickly head-fixed using a stereotaxic apparatus when they were anesthetized. Isoflurane

was maintained with a constant level of (0.75%) in O_2 (flow rate: 0.2 L/min) when the mice were stable. Temperature was maintained at 35°C with a heating pad. A small incision of the head skin was made to expose the area of the visual cortex. The skull of the recording area was ground thin, cleaned and covered with silicone oil. The recorded area was illuminated with the green light of 550 nm to obtain a brain vasculature map and the red light of 630 nm to acquire evoked responses. Images were captured using a Dalsa Pantera 1M60 CCD camera. Put UCLs on the mice's eyes, in the vision field of the eyes (15°, 45°,75° azimuth), visual stimulations of moving rectangular grating generated by 535-nm or 980-nm lasers were displayed. For each eye, cortical activity elicited at the stimulation frequency was calculated by Fourier analysis. In each session, a set of four images was taken by visualizing the response of the contralateral eye.

Light-induced conditioned place avoidance

To test whether NIR could mediate the decision-making behavior of mice with UCLs, a conditioned place avoidance experiment was performed.[47,48] A 26 cm × 13 cm × 13 cm custom box with a metal-rod bottom was made and a black board with a hole in the middle separated it into two boxes. On the surround of the other three sides of each box, 75 LEDs emitting at 535 nm or 980 nm (arranged in a 5 × 5 LED array on each side) were evenly placed for light stimulation. During the training stage, each mouse was placed in the box to distinguish two different kinds of stimulations from the two boxes and then make a decision. During the experiment, one of two stimulations was associated with punishment, specifically a foot electric shock administered using the metal-rod array. Correct decision-making by the mouse, either staying in or moving into another box with unpunished stimulation across the hole in the blackboard, enabled it to avoid the electric shock. Each stimulation-punishment pair was randomly assigned to either one of the two boxes. Each training trial consisted of 20 seconds of 535-nm LED light stimulation, followed by a 5-second 1 mA electric shock, and then a 20-second interval. Training usually lasted for 6-7 days: 2 sections per day and 20 trials per section. After about 12-14 sections of training, mice could avoid being punished successfully by learning the stimulation-cued punishment rule, the 535-nm light stimulation test lasted for 1 days. Then some of the trained mice were worn with UCLs by the binocular suture way. After 1-2 days of recovery, the same pattern stimulation was applied but in which 535-nm LEDs were changed into 980-nm LEDs as test stimulation. We mainly used avoidance correct rate and response time to evaluate if mice acquired the skills of distinguishing different stimulations based on behaviors of mice's movement into or staying in the unpunished box during light stimulation.

NIR temporal and spatial information discrimination of humans through UCLs

All LED optical tests were conducted in compliance with the National Standard of the People's Republic of China (GB/T 20145-2006), the International Electrotechnical Commission (IEC 62471:2006), and European Standards (EN 62471:2008) providing recommendations for permissible exposure limits of the LED light.

Visual sensitivity test

In this study, apart from the experiments conducted under ambient light conditions, the participants underwent dark adaptation for more than 30 minutes and the experiments were conducted in darkness. Each participant with or without UCLs was required to stare at a visible or NIR LED array panel with the dominant eye, and another eye was masked. Here, a chin rest was employed to stabilize the participant's head and maintain a fixed viewing distance. Visible or NIR light with different light power intensities through 535-nm or 980-nm LED light panels was designed to test the visual sensitivity of each participant under dark room and ambient light backgrounds (ambient light: 100 lux, 200 lux or 300 lux). The visual sensitivity test for each light power intensity consisted of 20 trials, and each trial involved two successive stimulations (no flash followed by a 100-ms flash or a 100-ms flash followed by no flash), with an auditory cue preceding each stimulation. Participants were required to determine the sequence of the two paired stimulations. In theory, the expected accuracy rate of random judgments by participants in this experiment or the subsequent experiments was (100/n) %, where "n" represented the number of available choices. The discrimination index was formulated as (participant's response accuracy - (100/n) %) / (100% - (100/n) %).

Flicker fusion frequency

Each test for a specific flickering frequency encompassed 10 trials. Each trial comprised two successive stimulations, either constant light (>10 kHz) followed by flickering light or flickering light followed by a constant light (>10 kHz), with each stimulation lasting for 2 seconds and featuring a 50% duty cycle. Prior to each stimulation, an auditory cue was presented. Similarly, participants were required to determine the sequence of the two paired stimulations. Light power intensities on the cornea for this test: 535 nm-90.63, 980 nm-1.86×10^8, unit-photons/μm^2/s.

NIR temporal information discrimination experiment

Variations in stimulation frequency and the number of flashes encoded different letters as follows: "a" - 2 flashes at 2 Hz, "b" - 2 flashes at 5 Hz, "c" - 3 flashes at 2 Hz, "d" - 3 flashes at 5 Hz, "e" – 4 flashes at 2 Hz, "f" - 4 flashes at 5 Hz. 8 Letter sequences were discriminated. Light power intensities on the cornea for single flash: 980 nm - 4.0×10^6, unit - photons/μm^2.

Spatial information discrimination experiment

A series of gratings made by visible and NIR light LED array. Participants were required to distinguish the movement direction of light gratings (vertical or horizontal) in random occurrences, 10 times for each direction. In the test, we used the parameter-spatial frequency for visual spatial recognition to characterize human spatial resolution. Spatial frequencies at a certain visual distance of ~70 cm were 1.08, 2.15, 3.23, 4.32, 5.40, 8.10, 12.22, 24.44, 34.91, 40.73, 46.99, 61.09, 81.45, 122.18 cycles per degree (c/d). To demonstrate whether participants with UCLs could distinguish pattern images, different paired pattern images (▬ VS ▌, S VS O,

Please cite this article in press as: Ma et al., Near-infrared spatiotemporal color vision in humans enabled by upconversion contact lenses, Cell (2025), https://doi.org/10.1016/j.cell.2025.04.019

△ VS □) were made by the visible and light LED arrays. Sizes of each paired shapes were suitable to ensure the same irradiation power intensities for each shape. Herein, areas of ━ and ┃ were 4 cm^2, areas of S and O were 4.87 cm^2 and areas of △ and □ were 6.2 cm^2. Participants distinguished each paired pattern images and the above light gratings at a certain distance of ~70 cm from their eyes with the wearable eyeglass system (Figure 4G). The system comprised three plano-convex lenses and a built-in flat UCL integrated into the optical path. Lens1 focused the NIR image into an inverted real image, which was projected onto the UCL for conversion from NIR to visible image. Lens2 then inverted the visible image back into an upright real image. Lens3 magnified the real image into the virtual image within a single focal length, while increasing the distance of the image from the human eye. The diameter of Lens1 was 18 mm, with a focal length f1 of 20 mm; the diameters of Lens2 and Lens3 were both 12.7 mm, with focal lengths f2 and f3 of 15 mm each. The distance between the focal points of Lens1 and Lens2, denoted as p1, was 52.06 mm, while the distance between the focal points of Lens2 and Lens3, denoted as p2, was 43.26 mm. The distance between the flat UCL and the focal point of Lens1, denoted as v1, was 20.69 mm, and it could also be adjusted based on the object distance. Accounting for the imaging effects of the wearable eyeglass system, the actual image distance for the light grating is set to 44.9 cm. Since the spatial frequencies represented by the gratings need to be corrected based on the visual distance (44.9 cm), they are adjusted by multiplying by the ratio 44.9/70. At a visual distance of 44.9 cm, the corrected spatial frequencies are as follows: 0.69, 1.38, 2.07, 2.77, 3.46, 5.20, 7.84, 15.67, 22.39, 26.12, 30.14, 39.18, 52.25, 78.37 cycles per degree (c/d). The 535-nm light power intensity of the visible image in this experiment was 886.3 photons/μm^2/s, and the 980-nm light power intensity of the NIR image was 9.33×10^9 photons/μm^2/s. Each pair of pattern images occurred randomly 20 times (10 times for each pattern image).

Human NIR color vision through tUCLs

All laser optical tests were conducted in compliance with the National Standard of the People's Republic of China (GB 7247.1-2012), International Electrotechnical Commission (IEC 60825-1:2007) and European Standards (EN 60825-1:2007) providing recommendations for permissible exposure limits of laser light.

Color matching experiment

Participants were required to observe the circular board in front of them at the range of 2° visible angle, which was a white frosted film stuck with the blank lens or with the flat tUCLs. The circular board was equally divided into two parts, with a black light barrier between the two parts. A series of monochromatic LED lights at the range of 400 nm - 700 nm illuminated on one part of the circular board. Composite light of red (R), green (G) and blue (B) light illuminated on another part of the circular board. Integrating spheres were used to ensure that the LED light was uniform. In the visible light test, three monochromatic LED lights (three primary colors, R: 654 nm; G: 543 nm; B: 452 nm) were employed as the adjustable composite light, facilitating the attainment of color matching with the individual monochromatic LEDs. When composite light couldn't match some monochromatic LED light, we added a compensating primary color light, mainly red (R), on the part of the monochromatic LED. The luminance of the compensating light was shown as negative values on the tristimulus chart (Figure 5F). By slowly adjusting the luminance of the compensating light and composite light, we could make the colors on both panels match. In the NIR light test, a composite light comprising three types of lasers with different wavelengths (1532 nm, 808 nm, 980 nm) was adjusted to achieve color matching with the individual monochromatic LEDs. These three types of lasers were combined into a single laser beam through the utilization of a fiber beam combiner and enlarged into a uniform, coherent spot using a beam expander to ensure consistent optical performance. The combined laser beam could be up-converted to composite light of red (R), green (G) and blue (B) light by the flat tUCLs. To ensure the safe use of lasers, a NIR cut-off filter with visible light transmittance was closely attached to the outer side of the flat tUCLs. Similarly, in the NIR color matching experiment, a compensating primary color light was added to the monochromatic LED part in some situations (Figure 5H). To determine the spectral tristimulus curve of CIE (International Commission on Illumination) 1931 RGB color space and color mapping of human's visible and NIR color vision, the light power intensity of each monochromatic LED light should be identical (5 nW/mm^2). In the corresponding visible composite light, the adjustable power intensity ranges were 0-19.37 nW/mm^2 for red light, 0-5.08 nW/mm^2 for green light, and 0-5.42 nW/mm^2 for blue light. In the NIR composite light, the ranges were 0-307.68 mW/mm^2 for 1532 nm light, 0-54.10 mW/mm^2 for 980 nm light, and 0-81.24 mW/mm^2 for 808 nm light. Meanwhile, the related luminance and chroma values of a series of monochromatic and composite light were measured by a spectrum-color-luminance meter (SRC-200S, EVERFINE Corporation). The spectral tristimulus values are standard color matching functions that describe human visual response to light at different wavelengths. They are calculated from measurements of three primary color-R/G/B luminance required to match series of iso-energetic monochromatic LED light, followed by normalization processes including normalization to the luminance value at 550nm (where human eyes are most sensitive) and standardization based on the relative luminance ratios to red color in R/G/B composite white light (Figure S5). The chromaticity diagram is a two-dimensional graph used to represent color properties, primarily displaying the hue and saturation of colors, but not the brightness information. In the chromaticity diagram, colors are typically represented by chromaticity coordinates, which are defined based on human perception of different wavelengths of light. For example, the CIE 1931 chromaticity diagram is widely used in color science, where it describes the position of a color using two coordinates (x and y). The edges of the chromaticity diagram usually represent different pure light colors (i.e., colors with the highest saturation), while the center of the diagram represents white, and the surrounding areas represent other colors, with varying hues and saturations. Chroma values of a series of monochromatic and composite light sources can be directly measured using a spectrum-color-luminance meter (SRC-200S, EVERFINE Corporation).

NIR color information discrimination experiment

While maintaining safe power intensity levels for the lasers, tUCLs were positioned approximately 1.0 cm away from the participants' eyes, and a tilted laser beam was utilized to ensure safety during laser application and avoid direct exposure. Furthermore, a NIR cut-off filter with visible light transmittance was employed to mitigate potential safety concerns. Firstly, participants were required to discriminate three primary colors - red, green and blue light. The corresponding output wavelengths of NIR RGB were 1532 nm, 808 nm and 980 nm. After observation, participants needed to make judgments about the sequence of RGB (6 groups of RGB sequences occurred randomly 30 times and 5 times for each group). According to color match experiments, 6 colors (red, yellow, green, cyan, blue, violet) were used to encode different letters, and 8 letter sequences were discriminated. In the discrimination experiments of NIR color and temporal coding information, six colors encoded different words including different kinds of subject, and predicate words, while three colors and different temporal frequencies (1 Hz, 2 Hz, 4 Hz) encoded object words. The duration of a single flash for subject and predicate words was 1000 ms, while each object word had a total of 1000 ms flashes with a 50% duty cycle. Corresponding words could be used to encode a complete sentence. Participants firstly learned the content of the encoded information, and make judgments. 63 sentences occurred randomly 315 times (5 times for each sentence). For all behavioral experiments related to colors, light power intensities of three primary colors in different composite colors were referred to associated light power intensities in color matching experiment. NIR light power intensities on the cornea were less than 10^7 photons/μm^2/s. The duration of a single flash for each color was 1000 ms.

Discrimination experiments for colorful pattern images

We selected the five composite colors and three pairs of pattern images (− VS |, S VS O, △ VS □) with equal areas to enable a comprehensive evaluation of perceptual performance. Sizes of each paired shapes were suitable to ensure the same irradiation power intensities for each shape. Herein, areas of − and | were 0.576 cm^2, areas of S and O were 0.136 cm^2 and areas of △ and □ were 0.12 cm^2. Participants distinguish paired colorful pattern images from a certain distance (70 cm) with the wearable eyeglass system. Each pair of colorful pattern images occurred randomly 50 times (5 times for each colorful pattern image).

Color reflection experiment

A light source reflection box was placed in front of participants, with reflective mirrors having different reflection spectra and a visible or NIR light source installed inside the box. The visible light was the composite white light composed of red (R), green (G), and blue (B) light, while the NIR light was the composite light that could produce a NIR white light effect on tUCL, formed by combining three types of NIR lasers (1532 nm, 808 nm, 980 nm) using a fiber optic beam combiner and beam expander (Figure 6A). By adjusting the intensity of the visible and NIR light, the luminance of the visible white light and NIR white light was ensured to be identical (0.4 cd/m^2). The visible white light or NIR white light was incident on the reflective mirror surface at an angle of 5°, and the reflected light could illuminate the area on the other side of the box. In this area, a white frosted board was placed, with a blank lens or tUCL adhered to it. We used a camera (Nikon-Z6) to take photos of the reflected light to characterize the actual colors of reflective mirrors seen by participants under the white light. At the same time, we used a UV-Visible-Near Infrared Spectrophotometer (Solid 3700 DUV) to measure the reflection spectra at a 5° incident angle of reflective mirrors and used a spectrum-color-luminance meter (SRC-200S, EVERFINE Corporation) to measure the chromaticity coordinates of the reflected light by reflective mirrors. In addition, we combined the tUCL-based wearable eyeglass system to capture the actual images of the letters "U", "S", "T", and "C" formed with different reflective mirrors under the illumination of visible white light and NIR white light. These letters were 6.5 mm in height, 5.3 mm in width, and had a line thickness of 1 mm.

QUANTIFICATION AND STATISTICAL ANALYSIS

Randomization and blinding

In all experiments, experimental animals were systematically randomized from multiple housing cages to ensure unbiased group allocation. Experimental animals were tested under a semi-randomized protocol, and the experimental and control animals were tested in turn. In all experiments comparing the conditions of wearing and not wearing contact lenses, the testing order was randomized to minimize sequence effects. The experimenters were partially unblinded during data collection and animal grouping, as they needed to record each animal's label. However, each data was analyzed by independent researchers using standardized parameters and algorithms.

Statistics reproducibility

Data are presented as the mean ± SEM or mean ± SD. Sample sizes are indicated in the figure' legends. Statistical differences of normally distributed data were determined using two-tailed Student's t-test. p values less than 0.05 were considered significant. p values are indicated as follows: $0.01 < *p < 0.05$, $0.001 < **p < 0.01$, $***p < 0.001$, n.s.: not significant.

ADDITIONAL RESOURCES

The clinical trial was registered and approved on the Chinese Clinical Trial Registry website (registered website: http://www.chictr.org.cn, registration number: ChiCTR2400082802).

Supplemental figures

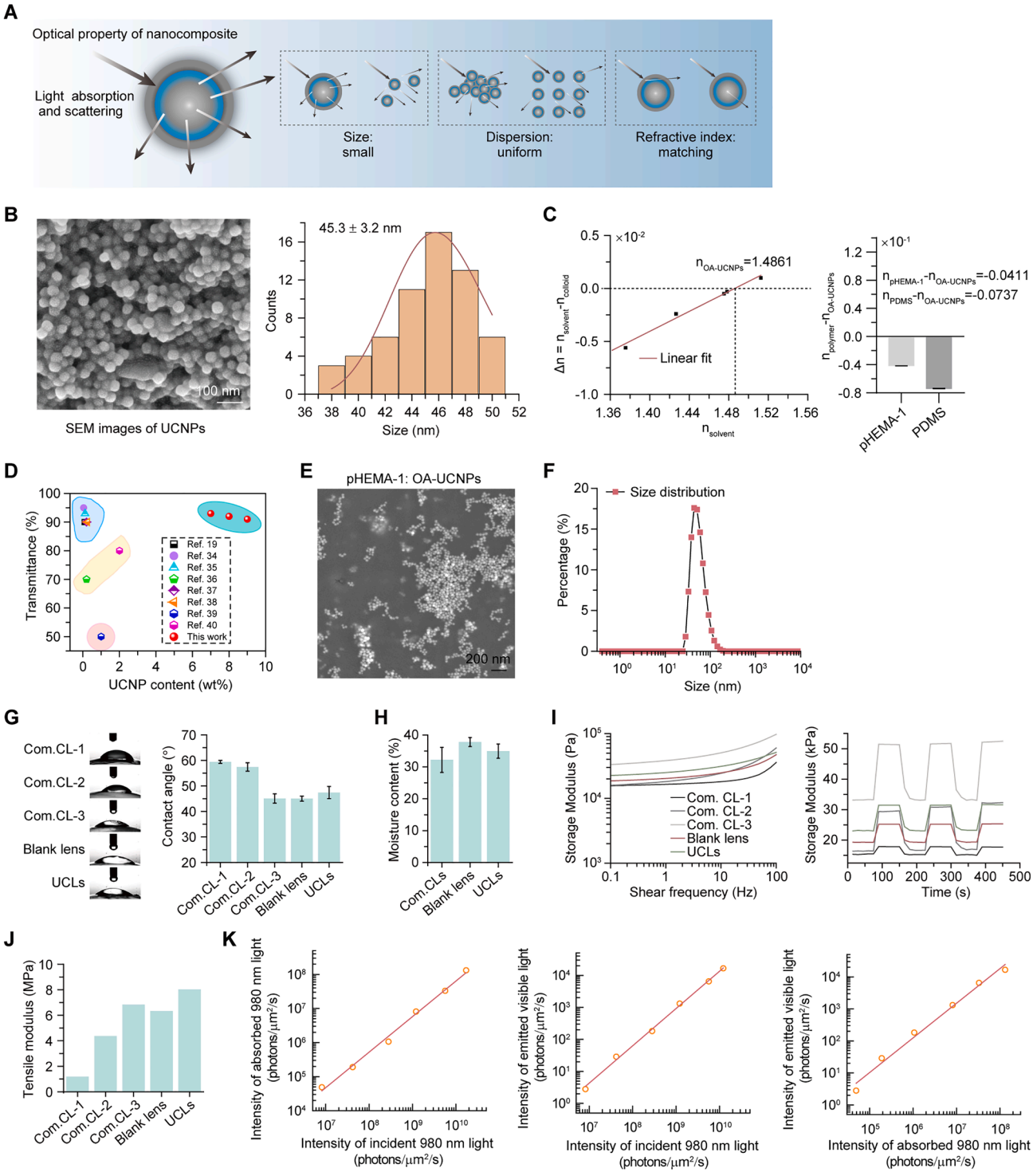

Figure S1. Screening strategy and some properties of UCLs, related to Figure 1

(A) Strategic screening of nanocomposites with high transparency.

(B) SEM images and size distribution of UCNPs (oleate-free).

(C) The refractive index difference of OA-UCNPs and polymers. Data are mean ± SD.

(legend continued on next page)

(D) Ashby diagram of nanoparticle mass contents vs. visible light transmittance for various reported UCNP/polymer film composites.[19,34–40]
(E) SEM image of the OA-UCNPs-fused pHEMA-1 contact lens. Oleate-coated and hydrophobic UCNPs were fused into the hydrophilic pHEMA-1 and dispersed very unevenly, causing a lower transparency level (Figure 1E).
(F) Hydrodynamic size distribution of UCNPs in mixed solutions. The hydrodynamic size distribution of UCNPs in the mixed solution before curing is measured by dynamic light scattering (DLS).
(G) Water contact angles on the surfaces of the UCLs and commercial contact lenses. The number of samples for each group was 3. Data are mean ± SEM.
(H) The water content of UCLs and commercial contact lenses. The number of samples for commercial contact lenses (Com.CLs), blank lens, and UCLs were 3, 4, and 5, respectively. Data are mean ± SEM.
(I) The rheological response and stability of various contact lenses under shear excitation. Clearly, all the storage modulus (G') of contact lenses increased as the shear frequency increased. Besides, the cyclic mechanical stability of contact lenses under the excitation of 0.1 and 10 Hz shear were also explored.
(J) Tensile modulus comparison of various contact lenses.
(K) The intensity of 980-nm light absorbed and visible light emitted after passing through UCLs under different intensities of incident 980-nm light. By measuring the intensity of 980-nm light after passing through a blank lens (contact lens without UCNPs) and UCLs under different intensities of incident 980-nm light, the absorbed 980-nm light intensity by UCLs can be calculated. The intensity of the emitted visible light is measured. These light intensity relationships are plotted on a log-log scale.

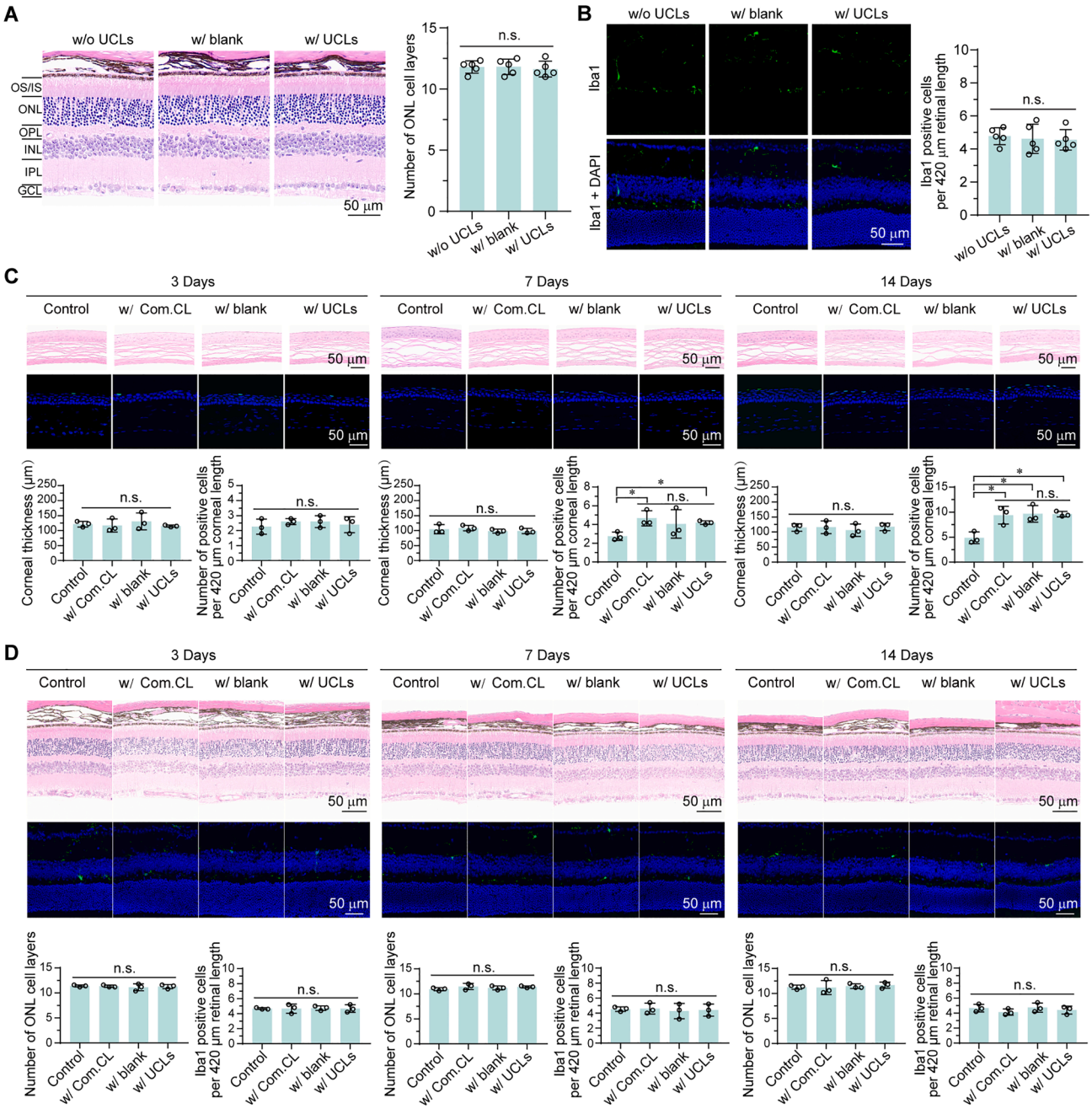

Figure S2. Long-term toxicological characteristics of UCLs on the corneas and retinae, related to Figure 1

(A) Retinal H&E staining and cell layer number in retinal outer nuclear layer of mice without UCLs, with blank or UCLs for 6 h. OS/IS, outer/inner segment of photoreceptors; ONL, outer nuclear layer; INL, inner nuclear layer; GCL, ganglion cell layer. Data are mean ± SD; two-sided t test; n.s., not significant.

(B) Iba1 staining of retinal slices of mice without UCLs, with blank or UCLs for 6 h. Green, Iba1; blue, DAPI. Scale bar, 50 μm. The number of positive cells per 420 μm retinal slice length was counted. Scale bar, 50 μm. Number of mice, $n = 5$ for all groups. Data are mean ± SD; two-sided t test; n.s., not significant.

(C) Corneal H&E staining and TUNEL staining were performed on the four groups of mice after 3, 7, and 14 days of wearing contact lenses (6 h per day). Green, TUNEL staining; blue, DAPI. Scale bar, 50 μm. The number of positive cells per 420 μm corneal length was counted. Control, without UCLs or commercial contact lenses; w/Com.CL, with commercial contact lens; w/blank, with contact lens without UCNPs fused; w/UCLs, with UCLs. Data are mean ± SD; two-sided t test; n.s., not significant; $0.01 < {}^{*}p < 0.05$.

(D) Retinal H&E staining and Iba1 staining were performed on the four groups of mice after 3, 7, and 14 days of wearing contact lenses (6 h per day). Green, Iba1; blue, DAPI. Scale bar, 50 μm. The number of positive cells per 420 μm retinal slice length was counted. Data are mean ± SD; two-sided t test; n.s., not significant.

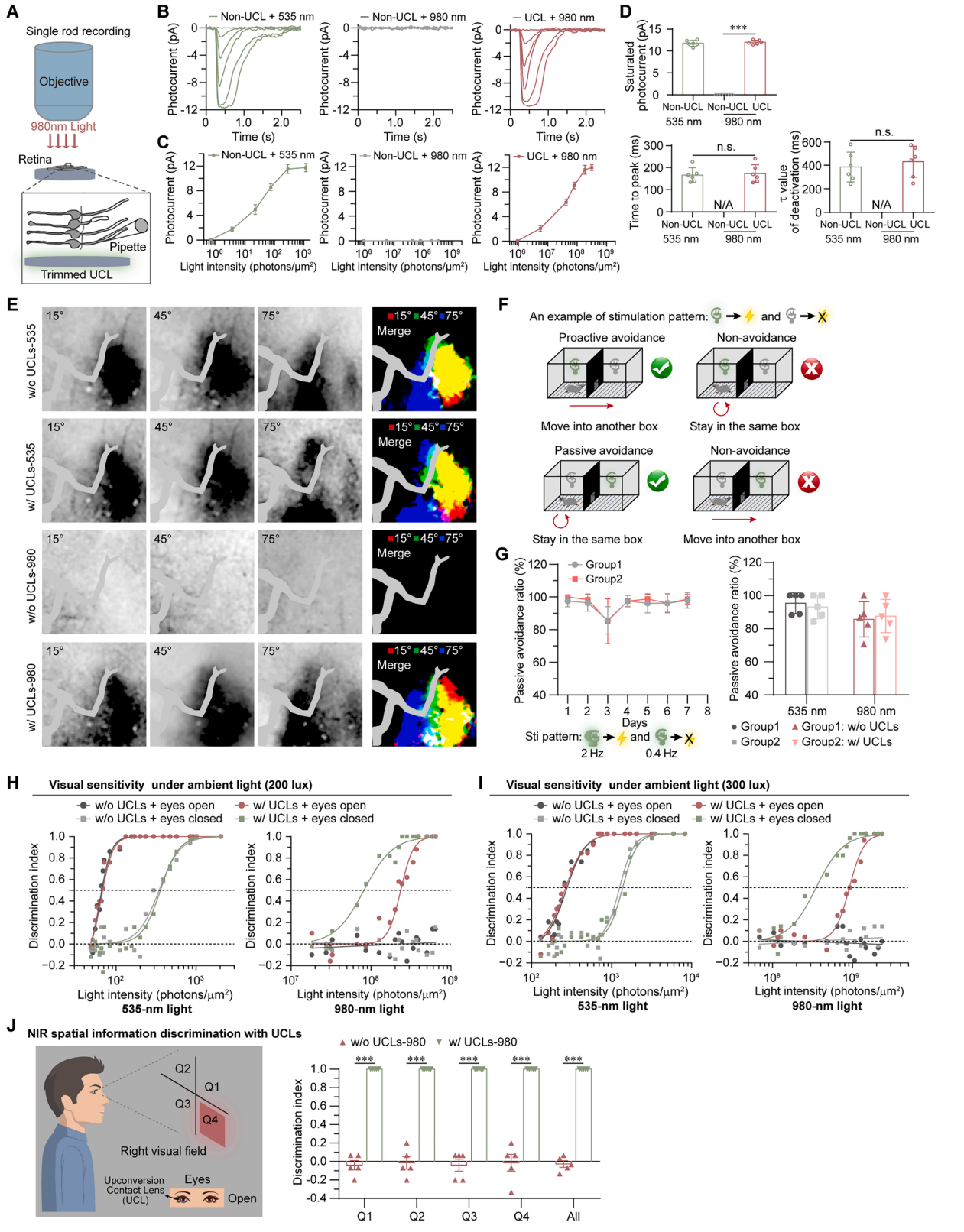

(legend on next page)

Figure S3. NIR-light-induced activation of photoreceptors and information discrimination in mice with UCLs and NIR-light sensitivity under brighter ambient light in humans with UCLs, related to Figures 2, 3, and 4

(A) A diagram of single rod recordings by directly attaching the UCL to photoreceptor cells.

(B and C) Photocurrents and intensity-response curves of rods with or without the UCL under 535- or 980-nm light stimulation. A series of photoreceptor responses were induced by 15-ms flashes of 535 or 980 nm at different intensities. Data were lowpass filtered at 50 Hz and sampled at 25 kHz by Axon 700B Amplifier and Digital 1440A interface. Photocurrent traces were averaged from 5 to 7 sweeps. Intensity-response data are mean ± SD.

(D) Saturated photocurrent of bright light response, time to peak and deactivation time constant of dim light response. Time to peak is the time from light stimulation to the peak amplitude of the dim light response. Number of recorded cells: non-UCL + 535 nm, $n = 6$; non-UCL + 980 nm, $n = 7$; UCL + 980 nm, $n = 6$. Data are mean ± SD; two-sided t test; n.s., not significant; N/A, not applicable; $^{***}p < 0.001$.

(E) Another example of the intrinsic optical imaging experiment. Intrinsic optical signals in the V1 cortex from mice with or without UCLs under visible light or NIR-light illumination. Overlapping images of intrinsic optical signals elicited in the V1 cortex by light grating stimulation are annotated with color to differentiate the responses at three distinct visual angles.

(F) The description of the conditioned place-avoidance experiment. Four distinct situations are presented. ''Passive avoidance'' refers to the situation where mice remain in the unpunished box passively when they are in the unpunished box at the start of light stimulation. ''Non-avoidance'' means that mice do not avoid the electric shock. Passive avoidance ratio = times of avoiding being shocked successfully/times of situations where mice were in the unpunished box when light stimulation started.

(G) Passive avoidance ratio of mice during the training and test stages. Data are mean ± SD.

(H and I) The NIR vision under brighter ambient light. Visual sensitivity to light power intensity of visible light and NIR light under 200 lux (H) and 300 lux (I) ambient light.

(J) NIR spatial information discrimination of humans with UCLs. Participants were required to distinguish the 980-nm NIR-light stimulus randomly appearing in the four quadrants (Q1–Q4) of the monocular visual field under dark conditions and to make judgments and responses. The 980-nm light stimulus appeared 10 times in each quadrant. Data are mean ± SEM; two-sided t test; $^{***}p < 0.001$.

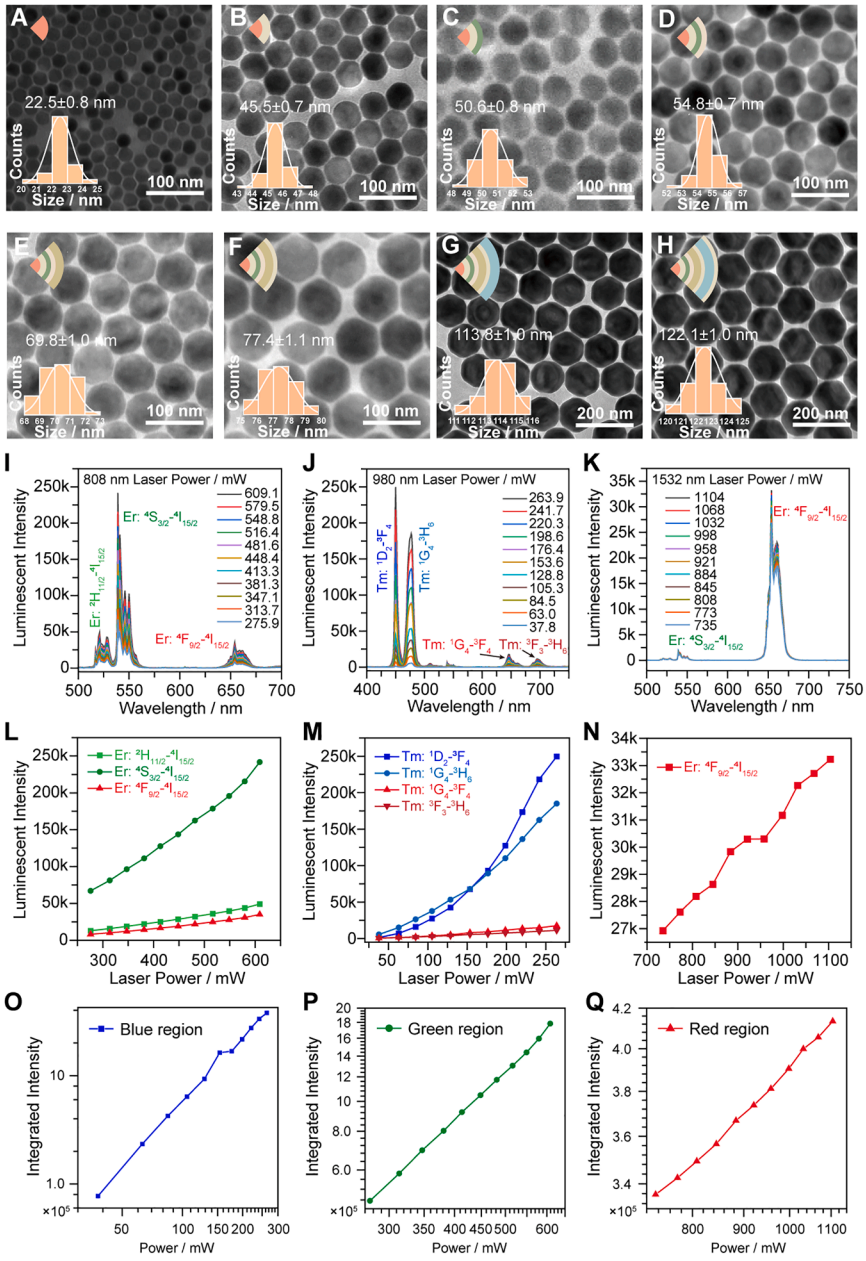

Figure S4. Size dispersion and luminescent upconversion spectra of trichromatic lanthanide nanoparticles, related to Figure 5

(A–H) Transmission electron microscope (TEM) images of the synthesized nanoparticles with each step from the experimental section. (A) Er core; (B) Er@Y; (C) Er@Y@2%Er; (D) Er@Y@2%Er@20%Yb; (E) Er@Y@2%Er@20%Yb@50%Nd, 20%Yb; (F) Er@Y@2%Er@20%Yb@50%Nd,20%Yb@Y; (G) Er@Y@2%Er@20% Yb@50%Nd, 20%Yb@Y@80%Yb, 1%Tm; (H) Er@Y@2%Er@20%Yb@50%Nd, 20%Yb@Y@80%Yb, 1%Tm@Y.

(I–N) Luminescent upconversion spectra of trichromatic lanthanide nanoparticles under different power intensities of laser excitation at wavelengths of 808, 980, and 1,532 nm.

(I and L) 808 nm laser mainly influenced the transition of Er $^4S_{3/2}$-$^4I_{15/2}$ (~540 nm). The transitions of Er $^2H_{11/2}$-$^4I_{15/2}$ (~520 nm) and $^4F_{9/2}$-$^4I_{15/2}$ (~654 nm) were less sensitive to the power change.

(J and M) The transitions of Tm $^1D_2$-$^3F_4$ (~450 nm) and Tm $^1G_4$-$^3H_6$ (~475 nm) were more dramatically affected by 980-nm laser than those in the red region.

(K and N) 1,532 nm laser had only effects on Er $^4F_{9/2}$-$^4I_{15/2}$ (~654 nm) within red emission.

(O–Q) The integrated intensity of (O) blue, (P) green, and (Q) red emission vs. different power of lasers excited by (O) 980, (P) 808, and (Q) 1,532 nm, respectively.

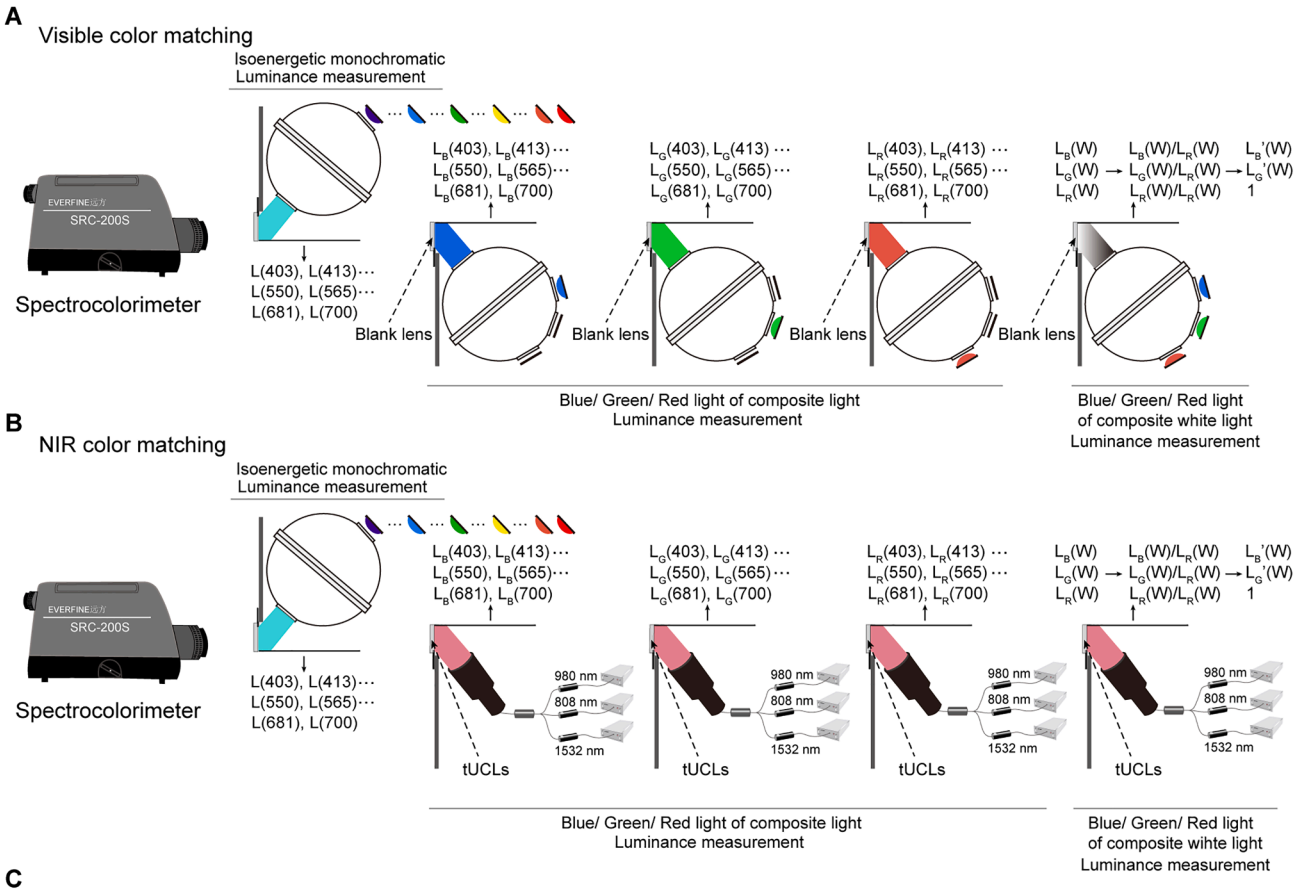

C

CIE1931 RGB spectral tristimulus values: $\bar{r}(\lambda) = L_R(\lambda) / L_{max}(550) / 1$

$\bar{g}(\lambda) = L_G(\lambda) / L_{max}(550) / L_G'(W)$

$\bar{b}(\lambda) = L_B(\lambda) / L_{max}(550) / L_B'(W)$ **Figures 5F and 5H**

Measured by spectrocolorimeter:

Chroma parameters of composite light ⟶ CIE1931 xy Chromaticity Diagram **Figures 5G and 5I**

Chroma parameters of isoenergetic monochromatic ⟶ CIE1931 xy Chromaticity Diagram **Figure S6B**

Figure S5. Methodology for conducting a color-matching experiment along with the associated procedures for data analysis and calculation, related to Figure 5

(A and B) Measurement procedure of color-matching experiment of visible and NIR light. Under the conditions of isoenergetic monochromatic LED light, the related luminance and chroma values of a series of monochromatic and composite light were measured and recorded by a spectrum-color-luminance meter. (C) Procedures of data analysis and calculation for spectral luminous efficiency curve, CIE1931 RGB spectrum tristimulus values, and xy chromaticity coordinates of composite light and isoenergetic monochromatic. L_{max}, representing the maximum luminance of the human spectral luminous efficiency curve,[66,67] corresponded to the luminance of monochromatic LED or composite light at a wavelength of 550 nm in this context.

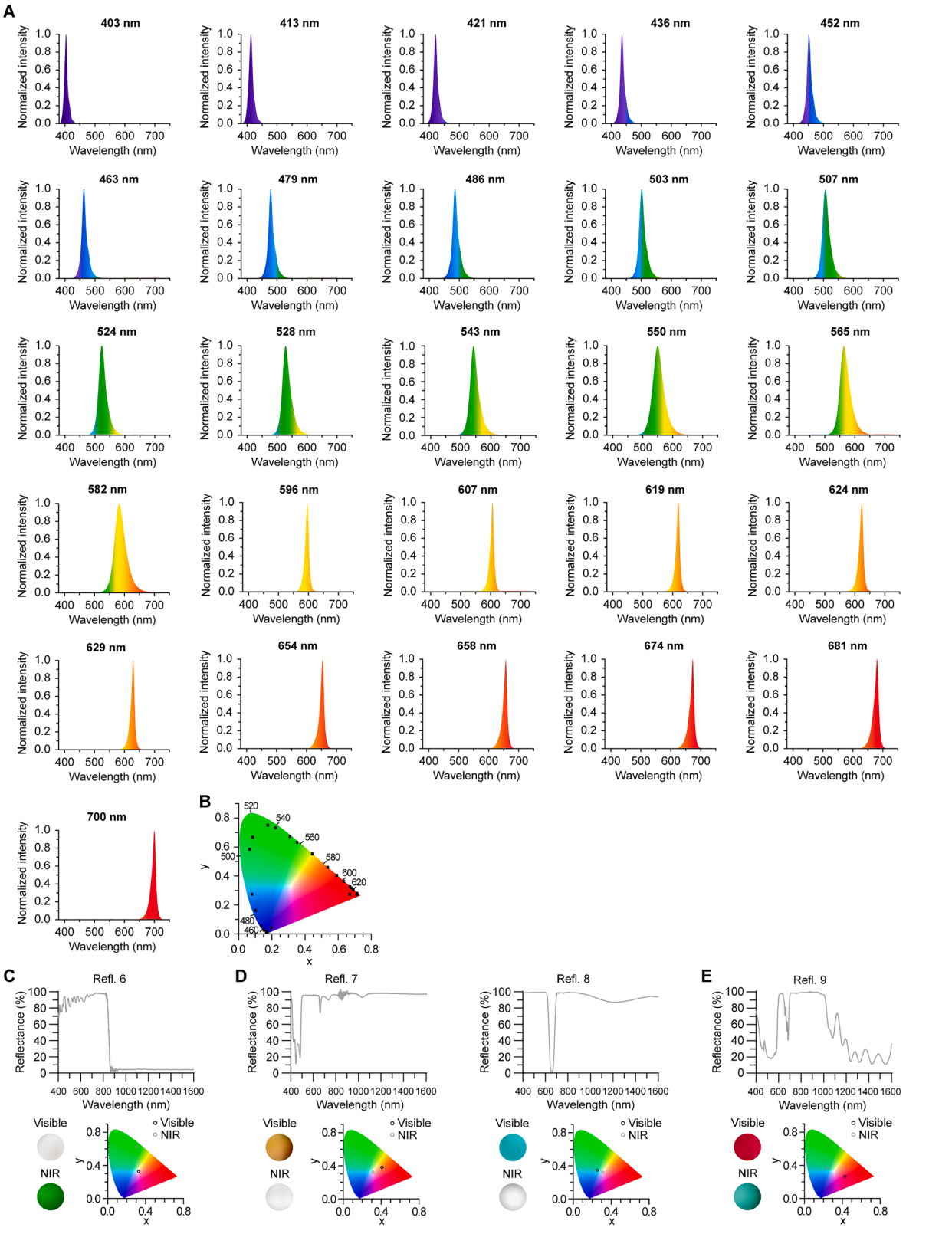

(legend on next page)

Figure S6. The spectra of monochromatic LEDs used in the color-matching experiment and the reflection of other different reflective mirrors, related to Figures 5 and 6

(A) Peak wavelength in the spectrum of each LED is presented, namely 403, 423, 421, 436 nm, etc. The light power intensities of each monochromatic LED light are identical (5 nW/mm^2).

(B) The xy coordinates on the CIE 1931 chromaticity diagram for these monochromatic LEDs were measured using a spectrum-color-luminance meter.

(C–E) The reflection spectra of other different reflective mirrors, the photographs displayed under visible white light and NIR white light, and the chromaticity coordinates on the chromaticity diagram.